Molecular Dynamics Studies of Anomalous Properties in Network-Forming Materials



Jesada Temaismithi

Linacre College

University of Oxford

A thesis submitted for the degree of

Master of Science (by Research)

September 2012

Abstract

Molecular dynamics simulations are used to investigate the anomalous properties, for instance, the density maxima, found in network-forming materials. In particular, we adopt the Polarisable-Ion Model (PIM) as the potential energy model used for the simulations. The advantage of employing this model is that only one parameter, the anion polarisability, is varied whilst others are kept fixed; therefore, we can systematically study how it affects these anomalous properties. The increase in the anion polarisability causes the change in the microscopic nature of the materials in that it decreases the average bond angle. This also leads to the change in the macroscopic properties in that it moves the regions of anomalies to lower temperature and higher density, which is towards the supercooled regime. However, the change in the anion polarisability does not affect the order of regions in the cascades of anomalies.

To Yeo Yong Kiat

Acknowledgements

First and foremost, I would like to acknowledge Dr Mark Wilson, my supervisor. I also owe thanks to Prof David Logan for the encouragement and assuring that I have enough to pursue research, in addition to actually making it possible by liaising with the Thai Government. I am also indebted to the Thai Government for the financial support.

The only other senior member of the group at the time, Stefan Craciun, was immensely helpful with all the technical details of the simulations. He was always keen to help and I am glad to have had him around. I would also like to thank Nattapong "Foam" Paiboonvorachat, the other post-graduate student who shared the office and a fellow Thai Scholar, for all the help and advice, both academic and personal, since before I came to Oxford.

I can perhaps say that I owe it all to Yeo Yong Kiat, who helps me recall how much passion I have for science, in addition to all the fun trips to the Continent. Thanks to my classmates, both Yeo Yong Kiat and Debayan Chakraborty for making me see very clearly how much luck plays a part in our lives and how lucky I was before.

Finally, a big thanks to mum, dad, and my brother for the love and for just being there listening and talking to me. It may be difficult to understand exactly what I have been doing every day away from home, but I do appreciate their understanding and the devotion of their time for me.

Declaration

I am the sole author of this thesis and have produced this thesis without making use of anything else other than those specified; other materials derived from articles or textbooks are properly acknowledged.

Jesada Temaismithi

Contents

List of Figures **vii**

List of Tables **xi**

1 Introduction **1**

2 Molecular Dynamics Simulations **3**

2.1 Classical Mechanics 3

2.2 Polarisable-Ion Model 5

2.3 Statistical Mechanics 7

2.4 Technical Details of the Simulations 8

2.4.1 Parameters for PIM 8

2.4.2 Simulation Conditions 8

2.4.3 Time Scale 9

2.4.4 Initial Configurations 10

3 Preliminary Results **11**

3.1 Relationship between P and T 11

3.2 Bond Angle Distribution 16

4 Order Parameters **21**

4.1 Translational Order Parameter 21

4.1.1 Definition 21

4.1.2 Results and Discussion 22

4.2 Orientational Order Parameter 27

4.2.1 Definitions 27

4.2.2 Results and Discussion 28

5 Diffusion **33**
5.1 Fick's Law and Diffusion Equation 33
5.2 Mean Squared Displacement Calculations 35
5.3 Results and Discussion 36

6 Isothermal Compressibility **41**
6.1 Definition 41
6.2 Thermodynamics of Supercooled Water 42
6.3 Methods of Estimation 44
6.3.1 Polynomial Fit of $P(V)$ 44
6.3.2 Number–Number Structure Factor 45
6.3.3 Number Fluctuation 52

7 Cascade of Anomalies **55**
7.1 Motivation from Liquid Water 55
7.2 Cascade of Anomalies 56
7.3 Discussion and Conclusions 58

References **63**

List of Figures

3.1 P–T plots for $\rho = 3.3$ g cm^{-3} 12
3.2 P–T plots for $\rho = 4.5$ g cm^{-3} 12
3.3 P–T plots for $\rho = 6.2$ g cm^{-3} 12
3.4 P–T plots for $\rho = 9.0$ g cm^{-3} 12
3.5 Construction of the TMD line 14
3.6 TMD lines on P–T plane 15
3.7 TMD lines on T–ρ plane 16
3.8 BAD for $\alpha = 0$ a.u. 18
3.9 BAD for $\alpha = 5$ a.u. 18
3.10 BAD for $\alpha = 10$ a.u. 18
3.11 BAD for $\alpha = 15$ a.u. 18
3.12 BAD for $\alpha = 20$ a.u. 18
3.13 BAD for $\alpha = 25$ a.u. 18
3.14 BAD for $T = 1500$ K 19
3.15 BAD for $T = 1100$ K 19
3.16 BAD for $T = 800$ K 19
3.17 BAD for $T = 500$ K 19

4.1 t for $\rho = 4.0$ g cm^{-3} 23
4.2 t for $\rho = 5.4$ g cm^{-3} 23
4.3 t for $\rho = 5.4$ g cm^{-3} 23
4.4 t for $\rho = 7.7$ g cm^{-3} 23
4.5 t for $\alpha = 0$ a.u. 25
4.6 t for $\alpha = 5$ a.u. 25
4.7 t for $\alpha = 10$ a.u. 25

4.8 t for $\alpha = 15$ a.u. . . . 25
4.9 t for $\alpha = 20$ a.u. . . . 25
4.10 t for $\alpha = 25$ a.u. . . . 25
4.11 Lines of t-minima on T–ρ plane . . . 27
4.12 q for $\rho = 4.0$ g cm^{-3} . . . 29
4.13 q for $\rho = 5.4$ g cm^{-3} . . . 29
4.14 q for $\alpha = 0$ a.u. . . . 31
4.15 q for $\alpha = 5$ a.u. . . . 31
4.16 q for $\alpha = 10$ a.u. . . . 31
4.17 q for $\alpha = 15$ a.u. . . . 31
4.18 Lines of q-maxima on T–ρ plane . . . 32
4.19 Regions of anomalous structural order . . . 32

5.1 Mean squared displacement as a function of time . . . 36
5.2 D of the anion for $\alpha = 0$, 5, 10 a.u. . . . 37
5.3 D of both the anion and the cation for $\alpha = 0$ a.u. . . . 38
5.4 D of both the anion and the cation for $\alpha = 10$ a.u. . . . 38
5.5 D for $\alpha = 0$ a.u. . . . 39
5.6 D for $\alpha = 5$ a.u. . . . 39
5.7 Regions of anomalous diffusivity . . . 40

6.1 Schematic representation of the TMD line and the spinodal line in P–T plane . . . 43
6.2 Partial pair distribution functions . . . 46
6.3 Faber–Ziman partial structure factors . . . 47
6.4 Bhatia–Thornton partial structure factors . . . 48
6.5 S_{NN} for $\rho = 4.0$ g cm^{-3} . . . 50
6.6 S_{NN} for $\rho = 5.4$ g cm^{-3} . . . 50
6.7 κ_T for $\rho = 4.0$ g cm^{-3} from 200 000-cycle MD simulations . . . 51
6.8 κ_T for $\rho = 5.4$ g cm^{-3} from 200 000-cycle MD simulations . . . 51
6.9 κ_T for $\rho = 4.0$ g cm^{-3} from 3 000 000-cycle MD simulations . . . 51
6.10 κ_T for $\rho = 5.4$ g cm^{-3} from 3 000 000-cycle MD simulations . . . 51
6.11 Relative Fluctuation for $\rho = 4.0$ g cm^{-3} . . . 54
6.12 Relative Fluctuation for $\rho = 5.4$ g cm^{-3} . . . 54

7.1 Cascade of Anomalies for liquid water 56
7.2 Cascade of Anomalies for $\alpha = 0$ a.u. 57
7.3 Cascade of Anomalies for $\alpha = 5$ a.u. 57
7.4 Cascade of Anomalies for GeO_2, BeF_2, SiO_2, and H_2O 60

LIST OF FIGURES

List of Tables

2.1 Parameters used in the short-range part (Fumi–Tosi form) of the potential energy function for the PIM 9

7.1 Densities and temperatures at the maximum of each line of anomaly 58

1

Introduction

Despite the ubiquity of tetrahedral network-forming materials in everyday life, ranging from the most biologically essential compound such as water [2] to the technologically useful compounds such as silica [21], scientists still have difficulty in understanding their anomalous behaviours [15]. Unlike crystalline solids, which have been extensively studied and have their foundations precisely laid out [1]—thanks to the short-range order present in such systems—it is much more difficult to understand liquids, in which there is a competition between directional attractions, such as the hydrogen bonds in water, and short-range repulsions.

The most standard example of the anomalous behaviours found in tetrahedral network-forming materials is perhaps the density maxima in water. In general, when a system at fixed pressure is cooled, one would expect the system to contract, which leads to an increase in density, and *vice versa*. However, upon cooling liquid water at atmospheric pressure, towards the freezing point, it exhibits density maximum at 4°C. In other words, whilst cooling liquid water from above 4°C leads to an increase in density as expected, cooling it further (below 4°C) leads to a decrease in density. This phenomena is usually attributed to the hydrogen bonds present in water. Since a number of inorganic melts, for instance, $ZnCl_2$, $GeSe_2$, etc., possess the same structural framework as that found in water, the microscopic and macroscopic properties of these salts are expected to be somewhat similar to those of liquid water.

The main tool used in this study is molecular dynamics simulation. Though anomalous properties of network-forming materials have been previously studied

[15, 20, 38], the simulations have focussed on individual systems, for instance, BeF_2, GeO_2, SiO_2, and H_2O. As a result, a direct comparison between different materials is problematic as the details of each model are different, in a *non*-systematic way. Therefore, we propose to use a single model with the hope of capturing the essence of anomalous properties by varying a single variable: the anion polarisability. Within the models we describe, the anion polarisability controls the angles between local coordinated polyhedra, i.e., it effectively controls the network topology. In this project, we follow the methodology of studying anomalous properties of network-forming material pioneered by Errington and Debenedetti [15].

The main goal of this project, therefore, is to use molecular dynamics simulations to study anomalous properties of network-forming materials. By varying only the anion polarisability, we hope to systematically investigate how it affects the anomalous properties, particularly, how the anion polarisability shifts the location of anomalous regions in the T–ρ plane.

This thesis is structured in the following manner: Chapter 2 presents all the necessary concepts associated with the main tool of study used in this project, the molecular dynamics simulation. Classical and statistical mechanics are briefly reviewed as necessary. Furthermore, the technical details of the simulations, for instance, the parameters used, the temperature and density range, and the time scale, are given at the end. We present the preliminary results, such as the calculated temperature and pressure, the P–T plots, and the bond angle distribution, in Chapter 3. These are direct results from the simulations.

Different anomalous properties are investigated in the later chapters. We begin by studying the translational and orientational order parameters in Chapter 4. Diffusion coefficient calculation and its anomaly are presented in Chapter 5. We have also included the calculations of the isothermal compressibility, despite the difficulty we faced in calculating them, in Chapter 6. It is this part of the study to which much time was dedicated, though unfortunately many problems could not be solved in time. It is also the part which motivates further investigation and correction of previous results. Finally, the cascades of anomalies are constructed with the goal of establishing how the anion polarisability, and hence the network topology, affects the different anomalous properties as a whole.

2

Molecular Dynamics Simulations

In order to investigate the physical properties of network-forming materials, including those that are anomalous, we choose to perform computational experiments using the technique of molecular dynamics (MD). The term *computational experiment* is used here because in order to perform a MD simulation, we need to set up a system of interest and vary certain parameters, such as density or temperature. In turn, we may obtain, though indirectly, certain physical properties, such as diffusion coefficients or isothermal compressibility, from the simulations.

Since a MD simulation is not costly—at least compared to performing an actual experiment, especially at extreme conditions such as high pressure and temperature—it can be used as an intial probe to systems of interest. Furthermore, various systems can be studied systematically—by varying only a certain variable whilst keeping others fixed—using MD simulations.

2.1 Classical Mechanics

Molecular dynamics is a computer simulation technique that utilises classical mechanics. The system of interest is composed of point particles, each of which located at a certain position in a box with a given initial momentum. To simplify the calculation, the boundary effects, for instance, the collisions between particles and the wall, are ignored by the use of periodic boundary conditions: the particles that move to the right of the box simply reenter it from the left and *vice versa*.

The dynamics of a particle is governed by the law of classical mechanics, i.e., Newton's Second Law:

$$\mathbf{F} = m\mathbf{a}, \tag{2.1.1}$$

where $\mathbf{F}$ is the net force acting on a particle with mass m, resulting in the acceleration, $\mathbf{a}$. The law can be rephrased in a more fundamental way:

$$-\nabla\mathcal{V} = \frac{\mathrm{d}\mathbf{p}}{\mathrm{d}t}, \tag{2.1.2}$$

where $\mathcal{V}$ is the potential energy, $\mathbf{p}$ is the momentum of the particle, and t is the time. The second equation has the advantage that it involves the more fundamental quantities: energy and momentum. In addition, the potential energy, which is a scalar quantity, is easier to keep track than force, a vector quantity.

The law of classical mechanics can also be recast in a Lagrangian formulation. The Lagrangian of a system of particles is defined as

$$\mathcal{L} = \sum_i \mathcal{T}_i - \mathcal{V}, \tag{2.1.3}$$

where $\mathcal{T}_i = \frac{1}{2}m_i\dot{\mathbf{r}}_i^2$ is the kinetic energy of the particle i whose mass is m_i and velocity $\dot{\mathbf{r}}_i$, and $\mathcal{V}$ is the total potential energy of the system. Lagrangian formulation of classical mechanics is based on Hamilton's Principle, which states that the path that a particle or a system of particles takes is that which minimises the action, defined as

$$\mathcal{S} = \int_{t_1}^{t_2} \mathcal{L}\,\mathrm{d}t. \tag{2.1.4}$$

Whilst the Lagrangian $\mathcal{L}$ is a function of the positions $\mathbf{r}_i$, and the velocities $\dot{\mathbf{r}}_i$, of the particles at time t, the action is a functional—a function whose input is also a function—of the position functions $\mathbf{r}_i(t)$ and velocity functions $\dot{\mathbf{r}}_i(t)$.

The Hamilton's Principle can be mathematically written as

$$\frac{\delta\mathcal{S}}{\delta\mathbf{r}(t)} = 0. \tag{2.1.5}$$

Using the technique of functional analysis, the condition (2.1.5) results in the Euler–Lagrange equations:

$$\frac{\partial\mathcal{L}}{\partial r_{i,\tau}} - \frac{\mathrm{d}}{\mathrm{d}t}\frac{\partial\mathcal{L}}{\partial\dot{r}_{i,\tau}} = 0, \tag{2.1.6}$$

where τ represents the different component (x, y, or z) of the position, $\mathbf{r}_i$, or the velocity, $\dot{\mathbf{r}}_i$, i.e., $r_{i,x} = x_i, \dot{r}_{i,x} = \dot{x}_i$. Assuming the potential energy of the system does not depend on the velocities $\dot{\mathbf{r}}_i$ of the particles, it is straightforward to show that the Euler–Lagrange equation leads directly to Newton's Second Law. Newtonian formulation and Lagrangian formulation of classical mechanics are thus equivalent.

Although nature at the atomic level is not well described by classical mechanics, *classical* molecular dynamics simulations are still widely used. By appropriately modifying the potential energy function used, we can inscribe quantum effects into the dynamics of the system. In other words, *classical* molecular dynamics with modified potential energy function can be used to correctly simulate microscopic systems. The modified energy function, usually referred to as the *effective potential energy*, is then tested by checking whether simulations with such potential energy functions reproduce properties found experimentally. Finally, despite the existence of quantum mechanical *ab initio* MD [9], classical MD requires much less computational resources due to the fact that *ab initio* MD requires the additional treatment of electronic states of the system of interest. In addition, classical models of the type used here may be systematically modified in order to study the evolution of properties of interest. Such systematic manipulation is difficult to attain with *ab initio* methods.

2.2 Polarisable-Ion Model

In MD simulations, each and every particle moves according to Newton's Law in the form expressed in equation (2.1.2). Therefore, one of the most essential ingredients of MD simulations is the model for potential energy function, $\mathcal{V}$.

The potential energy function used here is known as the *Polarisable-Ion Model* (PIM), developed by Madden and Wilson, and incorporates aspects of the many-body nature of the system [14, 23, 24, 46, 50]. The potential energy function of PIM consists of three terms:

$$\mathcal{V} = \sum_{i=1}^{N-1} \sum_{j=i+1}^{N} \left[U_{ij}^{\mathrm{sr}} + U_{ij}^{\mathrm{e}} \right] + \sum_{i=1}^{N} U_i^{\mathrm{ind}}. \tag{2.2.1}$$

The first term, U_{ij}^{sr}, is the short-range interaction between the ions i and j. The second term, U_{ij}^{e}, is the electrostatic interaction between the two ions. The last term, U_i^{ind}, is the energy required to polarise the ion i.

The short-range interaction, U_{ij}^{sr}, which is of Fumi–Tosi form, is composed of Born–Mayer short-range repulsion and London dispersion attraction [35]:

$$U_{ij}^{\mathrm{sr}}(r_{ij}) = B_{ij}e^{-a_{ij}r_{ij}} - \frac{C_{ij}}{{r_{ij}}^6}, \tag{2.2.2}$$

where a_{ij}, B_{ij} are the Born–Mayer constants, C_{ij} is the van de Waals coefficient, and $r_{ij} = |\mathbf{r}_i - \mathbf{r}_j|$ is the distance between the ions i and j.

The electrostatic interaction, U_{ij}^{e}, is the Coulombic energy and terms from multipole expansions, which we keep up to only the dipolar terms [8]:

$$U_{ij}^{\mathrm{e}}(r_{ij}) = T_{ij}(r_{ij})Q_iQ_j + \sum_{\tau} T_{ij,\tau}(r_{ij})\left(Q_j\mu_{i,\tau} - Q_i\mu_{j,\tau}\right) - \sum_{\tau,\sigma} T_{ij,\tau\sigma}(r_{ij})\mu_{i,\tau}\mu_{j,\sigma}, \tag{2.2.3}$$

where Q_i is the charge of the ion i, $\mu_{i,\tau}$ is the τ-component, $\tau \in \{x, y, z\}$, of the dipole induced on ion i, and T_{ij}, $T_{ij,\tau}$, and $T_{ij,\tau\sigma}$ are the components of the interaction tensors, with T_{ij} representing the Coulombic interaction between two point charges, $T_{ij,\tau}$ the interaction between a charge and a dipole, and $T_{ij,\tau\sigma}$ the interaction between two dipoles. The general form of the tensor is given by

$$T_{ij,\tau\sigma\rho\ldots}(r_{ij}) = \nabla_\tau\nabla_\sigma\nabla_\rho \ldots \frac{1}{r_{ij}}, \tag{2.2.4}$$

where ∇_τ is the τ-component of the gradient operator, i.e., $\nabla_\tau = \frac{\partial}{\partial r_{i,\tau}}$. For instance, consider the third term of U_{ij}^{e}, which is the interaction between the point charge i and the dipole j:

$$\sum_{\tau} -T_{ij,\tau}(r_{ij})Q_i\mu_{j,\tau} = \sum_{\tau} -\left(-\frac{(\mathbf{r}_i - \mathbf{r}_j)_\tau}{r_{ij}^3}\right)Q_i\mu_{j,\tau} = Q_i\left(\frac{\boldsymbol{\mu}_j \cdot \mathbf{r}_{ij}}{r_{ij}^3}\right). \tag{2.2.5}$$

The term in the last parenthesis is the potential field of a dipole. As expected, we obtain the interaction energy between a point charge i and a dipole j, $U = Q_i\Phi_j$.

The energy required to polarise the ion i, U_i^{ind}, can be written with the assumption that the induced dipole is parallel to the total field acting on the dipole, $\boldsymbol{\mu}_i = \alpha\mathbf{E}_i$, where α is the atomic polarisability [3]:

$$U_i^{\mathrm{ind}} = -\int \mathrm{d}\boldsymbol{\mu}_i \cdot \mathbf{E}_i = -\int \mathrm{d}\boldsymbol{\mu}_i \cdot \frac{\boldsymbol{\mu}_i}{\alpha} = -\frac{\mu_i^2}{2\alpha} \tag{2.2.6}$$

Furthermore, since the PIM has introduced the additional variable, the dipole moment $\boldsymbol{\mu}_i$, to the system, it is necessary to modify the kinetic energy function so that the Euler–Lagrange equation (2.1.6) can be used to describe the dynamics of the dipole moment $\boldsymbol{\mu}_i$. The kinetic energy is chosen to be

$$\mathcal{T} = \frac{1}{2}\sum_{i=1}^{N} m_i \dot{\mathbf{r}}_i^2 + \frac{1}{2}\sum_{i=1}^{N} M_i \dot{\boldsymbol{\mu}}_i^2. \tag{2.2.7}$$

The first term of the kinetic energy function is the real kinetic energy of the system: the sum of the kinetic energy of all particles, each with mass m_i, moving with velocity $\dot{\mathbf{r}}_i$. The second term is the additional term corresponding to the additional dipole moment degree of freedom. Analogously, M_i is the inertial parameter for the dipole and $\dot{\boldsymbol{\mu}}_i$ is the dipole velocity, i.e., how fast the magnitude and direction of each dipole moment $\boldsymbol{\mu}_i$, is changing.

Upon substituting the potential energy function (2.2.1) and the kinetic energy function (2.2.7) into the Euler–Lagrange equation (2.1.6), and changing the position variable $r_{i,\tau}$, to the dipole moment variable $\mu_{i,\tau}$, the following equation of motion for the dipole moment is thus obtained:

$$M_i \ddot{\mu}_{i,\tau} = -\sum_{j\neq i}\left[T_{ij,\tau}(r_{ij})Q_j - \sum_{\sigma} T_{ij,\tau\sigma}(r_{ij})\mu_{j,\sigma}\right] + \frac{\mu_{i,\tau}}{\alpha}. \tag{2.2.8}$$

2.3 Statistical Mechanics

Molecular dynamics simulations require the initial positions and momenta of all the particles, in addition to other parameters, as the input. The dynamics of the system is governed by the Euler-Lagrangian equation (2.1.6). This directly modifies the positions and momenta of all particles as the simulation progresses. The output of the simulations is therefore positions and momenta of all particles at each and every step of the simulations, which are not immediately useful. However, these microscopic properties are related to the macroscopic thermodynamic properties by statistical mechanics.

For instance, consider a single-component system. The pressure of such a system is related to the Helmholtz free energy, A, by the thermodynamics relation:

$$P = -\left(\frac{\partial A}{\partial V}\right)_{N,T}, \tag{2.3.1}$$

whist statistical mechanics relates the thermodynamic Helmholtz free energy to the canonical partition function, Z, via

$$A = -kT \ln Z. \tag{2.3.2}$$

The equation (2.3.2) is useful since the partition function and its appropriate derivative can be calculated from microscopic properties. Specifically, pressure can be calculated from the following equation[1]:

$$P = \rho kT - \frac{\rho^2}{6} \int_0^\infty r \, \frac{\mathrm{d}\mathcal{V}(r)}{\mathrm{d}r} \, g(r) \cdot 4\pi r^2 \, \mathrm{d}r, \tag{2.3.3}$$

where $\mathcal{V}(r)$ is the pair potential energy function, $g(r)$ is the radial distribution function, which is directly calculated from the positions of all particles.

2.4 Technical Details of the Simulations

In this section, technical details of the simulations are given. The details of the parameters used in PIM are given first, followed by the time scale and the system size studied in this project.

2.4.1 Parameters for PIM

For the Polarisable-Ion Potential Model of the type outlined above, equation (2.2.1), the short-range part of the potential energy function, equation (2.2.2), requires three parameters: $B_{ij}, a_{ij},$ and C_{ij}. These paramaters are used to model the $ZnCl_2$ system [17, 31, 47, 48, 49], though in the context of this project, they are chosen as they produce a generic tetrahedral network as is required for our investigation. Values of the parameters $B_{ij}, a_{ij},$ and C_{ij} are reproduced in Table 2.1 [37]. Formal valence-motivated charges (Zn^{2+} and Cl^-) are used throughout.

2.4.2 Simulation Conditions

Two physical variables that are varied systematically are temperature and density. The density variable is varied by changing the simulation cell size whilst keeping

[1] See page 188-190, section 30, chapter 6 in [19] for full derivation.

ij	B_{ij}	a_{ij}	C_{ij}
ZnCl	43.72	1.600	44
ClCl	87.00	1.556	183

Table 2.1: Parameters used in the short-range part (Fumi–Tosi form) of the potential energy function for the PIM. All values are listed in atomic units.

the number of particles in the system fixed. Since the goal of the project is to investigate the anomalous properties, the simulations are performed at the conditions such that anomalous behaviour can be observed. Most importantly, since we hope to systematically study how the anion polarisability affects both the immediate microscopic properties, such as bond angle distributions and mean coordination numbers, and the macroscopic properties, such as the equation of states and different anomalous properties, the anion polarisability α, is also varied in the range of 0 to 25 atomic units (a.u.), with the increment of 5 a.u.

For simulations with no polarisability—$\alpha = 0$ a.u., which is also called Rigid-Ion Model (RIM)—the range of temperature is 1100–2500 K and that of density is 3.14–7.73 g cm^{-3}; 600–2000 K and 3.14–7.73 g cm^{-3} for $\alpha = 5$ a.u.; 300–1500 K and 3.96–10.61 g cm^{-3} for $\alpha = 10$ a.u.; and 400–800 K and 5.43–10.61 g cm^{-3} for $\alpha = 15$, 20, and 25 a.u. All simulations are performed with a fixed total number of 324 particles. Note that for the latter sets of simulations, the lowest temperature investigated is 400 K; the liquid may rapidly crystallise at lower temperature.

2.4.3 Time Scale

In addition to studying what effects the variation of temperature, pressure, and polarisability have on microscopic and macroscopic properties of network-forming materials, the simulations are also performed at two different time scales. The universal time step increment used in this project is 25 a.u. ≈ 0.6 fs. The first set of simulations is performed for 200 000 MD steps ≈ 0.1 ns during equilibrating period and another 200 000 steps during data gathering period. The simulation with the smallest system size ($L = 40$ a.u. or $\rho = 7.73$ g cm^{-3} at $T = 1100$ K) takes approximately 10 hours of actual run time for RIM and 40 hours for PIM.

The second set of simulations is performed for 3 000 000 steps $\approx$ 2 ns during equilibrating period and another 1 500 000 steps $\approx$ 1 ns during data gathering period. The simulation with the smallest system size (same condition as before) takes the total of 6 days of actual run time for RIM and 20 days for PIM. Due to limited computational resources, both sets of simulations were run for those with $\alpha = 0, 5,$ and 10 a.u.

2.4.4 Initial Configurations

The initial configuration of $ZnCl_2$ used is that of a crystal. Before any simulations were carried out, the solid is melted at high temperature. The resulting configuration is then used as an initial configuration for RIM. After the simulations, both the equilibrium part and the data gathering part, the resulting configuration of the liquid $ZnCl_2$ is used as an initial configuration for PIM with $\alpha = 5$ a.u. The process is subsequently repeated as the polarisability is increased, assuming that the structures of the systems with closer polarisability are more similar.

3

Preliminary Results

Before we begin to investigate the anomalies in different physical properties, both static and dynamical, in this chapter, we present the results of the molecular dynamics simulations that have been carried out. This includes the relationships between pressure, temperature, and density, and the bond angle distribution. The main purpose of this chapter is to study how the anion polarisability affects the elementary macroscopic properties, e.g., temperature, pressure, and density, and microscopic geometric properties, with the hope that they will later be useful in determining the relations between geometric properties and different anomalous properties. Finally, since the anomalies in density are clearly observed in the P–T plots, the discussion of density anomalies is included in this chapter as well.

3.1 Relationship between P and T

We begin by presenting examples of P–T plots. Figure 3.1–3.4 show the system pressures as a function of temperature for systems at four different densities: 3.3, 4.5, 6.2, and 9.0 g cm^{-3}. At each density, different values of anion polarisability are considered. When temperature is sufficiently high, in all cases, the system pressure rises with increasing temperature. This is intuitive in a sense that by heating a system, particles in that system gain kinetic energy, resulting in more collisions per unit time with the system boundary; thus, the pressure of the system increases. In some cases, however, anomalous behaviour is observed, in

which pressure falls with increasing temperature resulting in a minimum in the P–T plot. As the anion polarisability is increased, at fixed density, the temperature at which P–T minimum is observed appears to fall. In a number of cases, the temperature of the minimum appears to fall to temperatures which are effectively inaccessible to our simulations, with ion dynamics too slow to effectively observe observe any relaxation on typical simulation time scales. Indeed, the effect of the lowering of temperature can be seen in the more erratic behaviour of the P–T curves at low temperature. Since our primary interest is in locating the P–T anomaly, we restrict ourselves to plotting data for polarisabilities, in which such anomalies are observed.

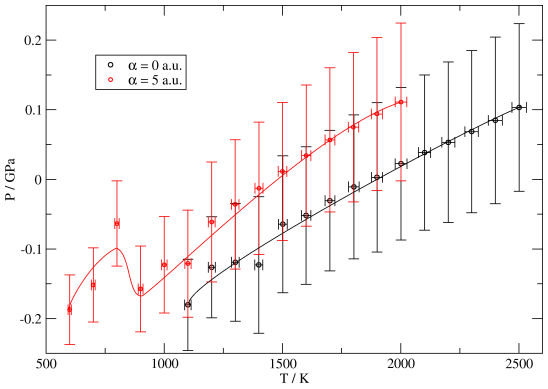

Figure 3.1:
P–T plots for $\rho = 3.3$ g cm^{-3}

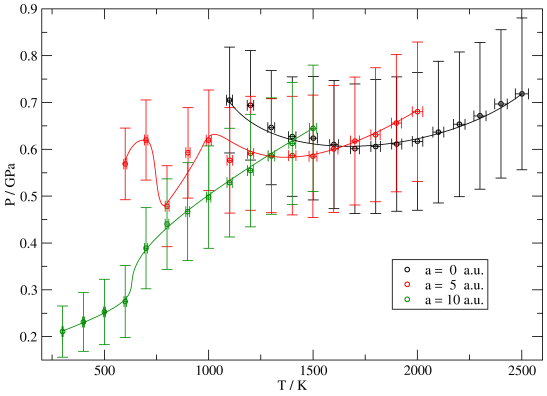

Figure 3.2:
P–T plots for $\rho = 4.5$ g cm^{-3}

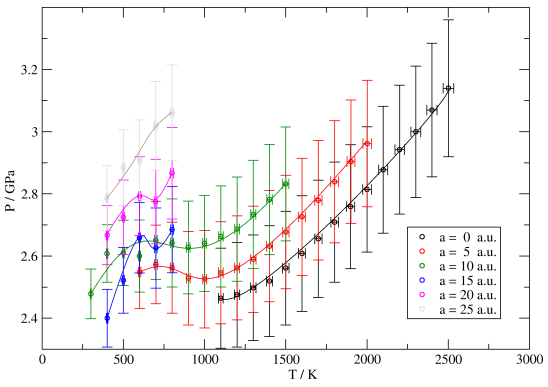

Figure 3.3:
P–T plots for $\rho = 6.2$ g cm^{-3}

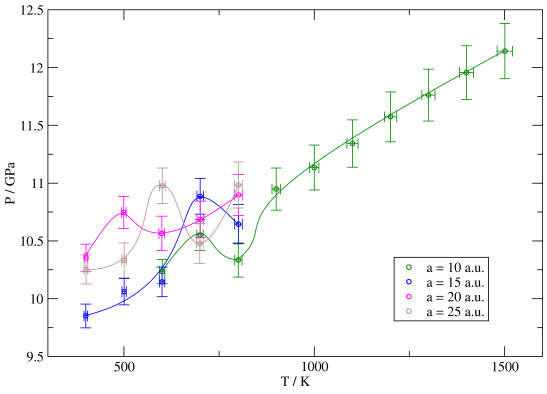

Figure 3.4:
P–T plots for $\rho = 9.0$ g cm^{-3}

A very well-known anomalous property of interest is the "temperature of maximum density" (TMD) [29]. Since we have studied the relationship between pressure and temperature of the system, we may proceed to investigate how such a relationship may help us understand the relationship between density and temperature, and eventually extract information with regard to the TMD. As temperature of a system increases, the particles gain kinetic energy and normally resulting in an expansion of the system. Therefore, as temperature of a system increases, we expect that the density decreases. If there exists an anomalous region—a region in which the increase in temperature results in decreasing pressure and increasing density—at low temperature, then there must a point at which density reaches a local maximum; the temperature at which this is the case is called the TMD. As the pressure is varied, the loci of the TMD form a line, which is referred to as the TMD line. In order to construct a TMD line, theoretically, one needs to first locate the TMD of a system at fixed pressure by varying temperature. Then, by obtaining the TMD at different pressures, we can construct the TMD line. Alternatively, the TMD line may be constructed from simulations performed at fixed density.

By definition, the density is maximised on the TMD line, i.e.,

$$\left(\frac{\partial \rho}{\partial T}\right)_P = 0. \tag{3.1.1}$$

Consider the cyclic rule of the three variables, P, T, and ρ:

$$\left(\frac{\partial P}{\partial T}\right)_\rho = -\left(\frac{\partial \rho}{\partial T}\right)_P \left(\frac{\partial P}{\partial \rho}\right)_T \tag{3.1.2}$$

$$= -\left(\frac{\partial \rho}{\partial T}\right)_P \frac{1}{\rho \kappa_T} \tag{3.1.3}$$

$$= 0, \tag{3.1.4}$$

where κ_T is the isothermal compressibility. In going from the equation (3.1.2) to (3.1.3), we have used the following relation:

$$\left(\frac{\partial \rho}{\partial P}\right)_T = \left(\frac{\partial (N/V)}{\partial P}\right)_T = \frac{N}{V} \cdot -\frac{1}{V}\left(\frac{\partial V}{\partial P}\right)_T = \rho \kappa_T. \tag{3.1.5}$$

Since both the density, ρ, and the isothermal compressibility, κ_T, are non-zero, equation (3.1.4) follows immediately from the TMD condition (3.1.1). In addition, since ρ and κ_T are positive quantities, equation (3.1.3) implies that, in a particular region, if the increase in temperature at fixed pressure results in density decrease, then the increase in temperature at fixed density must be accompanied by pressure increase, and *vice versa*. Therefore, the TMD, or the temperature of *maximum* density, is equivalent to that of *minimum* pressure. Finally, we conclude that in order to identify the TMD loci, we shall first find the pressure minima for simulations with varying temperature at fixed density. Then, by varying density, we will be able to construct the TMD line. Figure 3.5 shows how the TMD line may be constructed for a single model (here, the RIM, for which $\alpha = 0$ a.u.) by performing simulations over a range of densities.

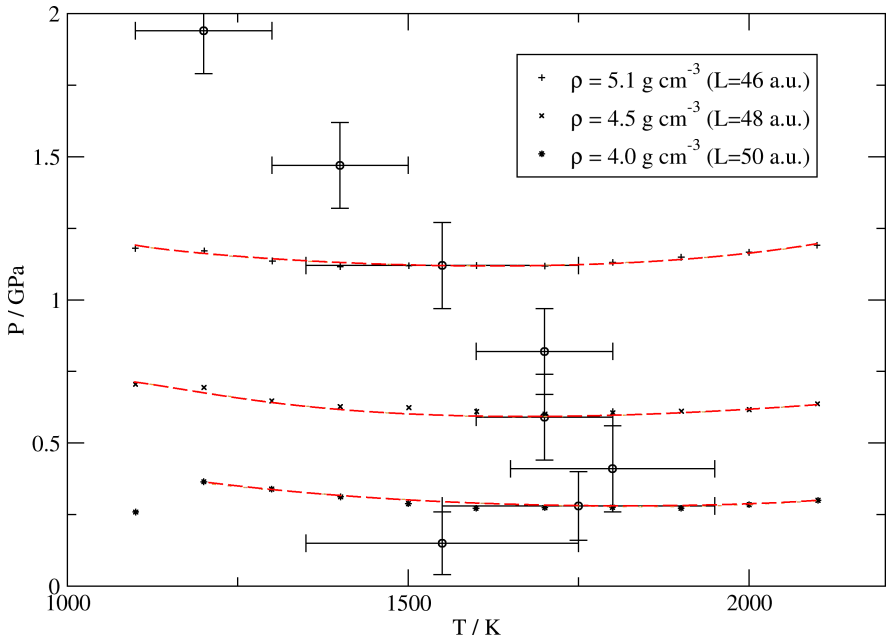

Figure 3.5: Construction of the TMD line for RIM. In order to determine the TMD for a system with fixed density, temperature is varied (red dashed lines, shown for 3 densities) and the pressure minimum is located (points with error bars, shown for 8 densities). The TMD line is constructed from the TMD for different densities.

By varying the anion polarisability, we can construct the TMD lines for different systems (Figure 3.6). The data sets presented are those from RIM and

PIM with $\alpha = 5$ a.u.; those with higher anion polarisability do not clearly show density anomaly. Clearly, the polarisability increase shifts the TMD line to lower temperature and higher pressure, and the curvature of the line is reduced. By estimating the location of the minima in P–T plot for $\alpha = 10$ a.u., it appears that the TMD line moves up to pressure as high as 5 GPa and temperature as low as 800 K, which is in the solid region of the phase diagram of $ZnCl_2$ [7]. In addition, the curve appears almost vertical; its curvature is very low.

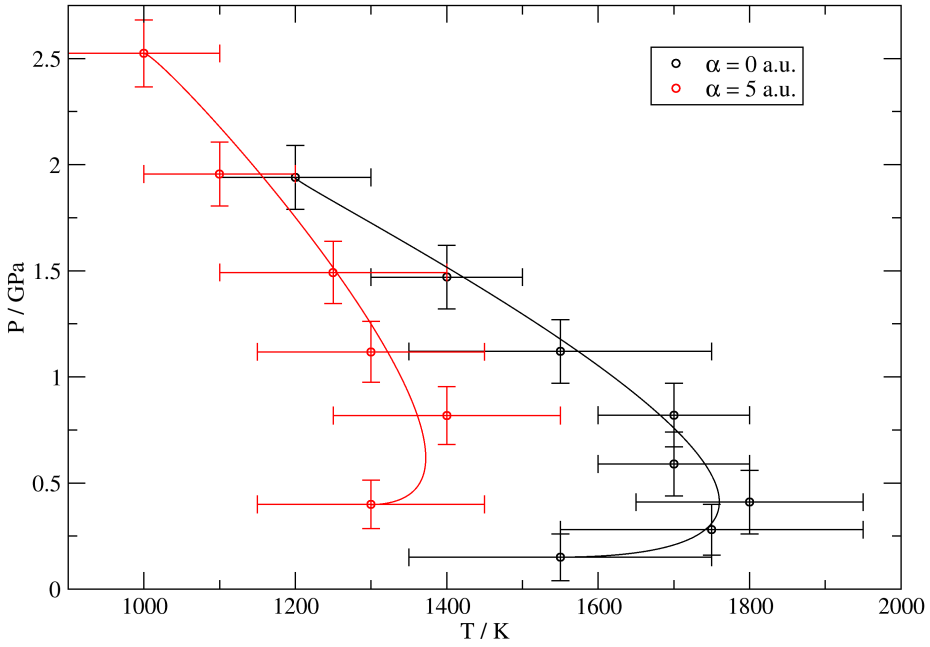

Figure 3.6: TMD lines on P–T plane. Lines are shown for $\alpha = 0$ a.u. (RIM—black line) and $\alpha = 5$ a.u. (red line).

Alternatively, we can construct the TMD line on T–ρ plane (Figure 3.7), instead of P–T plane, which will be useful later in the discussion of different types of anomalies. The increase of the polarisability shifts the TMD line to lower temperature and higher density, analogous to the behaviour found in Figure 3.6, which shows that the TMD line is shifted to lower temperature and higher pressure. In this plot, there is no fluctuation in density as all simulations are performed with fixed number of particles in a periodically bounded box.

3.2 Bond Angle Distribution

In order to study how microscopic properties of network-forming materials relate to macroscopic properties, we begin by calculating the bond angle distribution (BAD) for systems with varying anion polarisabilities. We focus on the angle about the anion, i.e., the M–X–M angle, as this angle controls the spatial relationship between nearest neighbour coordination polyhedra and hence controls the system topology.

Figure 3.8–3.13 show how bond angle distributions vary with temperature at different polarisabilities; the densities of these systems are kept fixed at 5.4 g cm^{-3}. At low polarisabilities, we observe peaks at obtuse angles, located at about 120°–150°. As temperature increases, the peaks shift towards lower angle, and the bond-angle distribution appears broader, especially in the case of $\alpha = 0$ and 5 a.u. (Figure 3.8 and 3.9). The fact that the variances of these distributions increase implies that as temperature increases, the system becomes more disordered. This observation can be explained by considering the minimisation of free energy, which is composed of enthalpy and entropy. At high temperature,

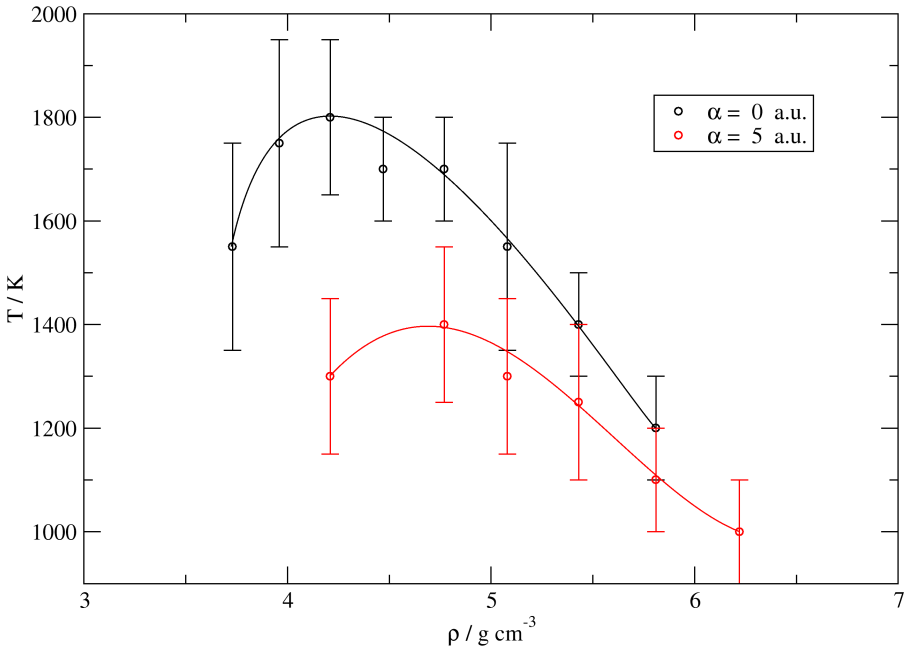

Figure 3.7: TMD lines on T–ρ plane. The key is the same as in Figure 3.6.

the entropy term is more important, and free energy is minimised by maximising the entropy. Hence, it is expected that the system is more disordered and has broader distribution at high temperature.

Once the anion polarisability is sufficiently large, another set of peaks at acute angles, located at about 80°–90°, starts to develop as a weak shoulder for $\alpha = 10$ a.u. (Figure 3.10), and becomes obvious for $\alpha = 15$ a.u. (Figure 3.11) and higher. This is due to the increase in the presence of edge-sharing tetrahedral units in the system [51]. When polarisability is increased, the intensities of the obtuse-angle peaks are decreased whilst those of acute-angle peaks are increased (Figure 3.12). In fact, the obtuse-angle peaks almost disappear when polarisability is increased to 25 a.u. (Figure 3.13).

Finally, in order to clearly observe how anion polarisability affects the bond angle distribution, plots for systems at fixed temperature and density, with only polarisability varied, are created. Figure 3.14–3.17 show the BAD for systems fixed at a density of 5.4 g cm^{-3}, at 1500, 1100, 800, and 500 K, respectively. Note that at high temperature (Figure 3.14 and 3.15), only systems with low polarisabilities are simulated; the temperature range for the systems with high polarisability, in which anomalous properties are observed, is lower than 1000 K. At high temperature, since the polarisability is low, only the obtuse-angle peaks are observed. At low temperature (Figure 3.16 and 3.17), however, both types of peaks are observed. Additionally, it is also clear from these two figures that as polarisability is increased, the intensities of the acute-angle peaks are increased, which corresponds to the increasing number of edge-sharing units. Furthermore, the increase in polarisability also decreases the magnitudes of angles of both types of peaks. This is to be expected as the induced dipole moment on the anion effectively bends the X–M–X bond; the higher the polarisability, the stronger the dipolar field, the stronger force on the M^{2+} ion, and the smaller the bond angle.

In conclusion, by increasing the anion polarisability in the molecular dynamics simulations, we effectively increase the number of edge-sharing tetrahedral units and decrease the magnitude of both types of angles.

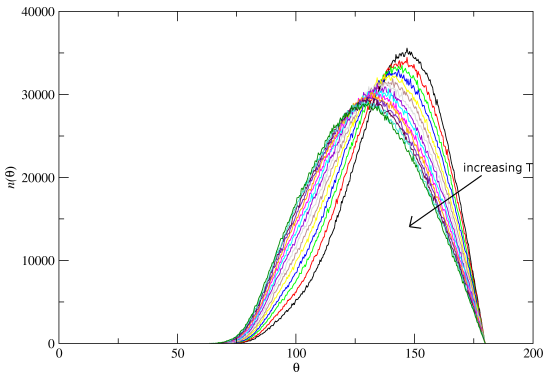

Figure 3.8: BAD for $\alpha = 0$ a.u.

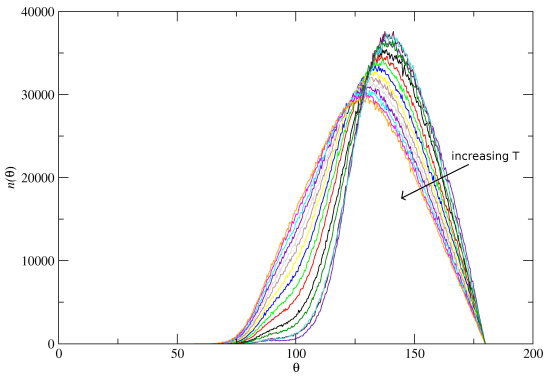

Figure 3.9: BAD for $\alpha = 5$ a.u.

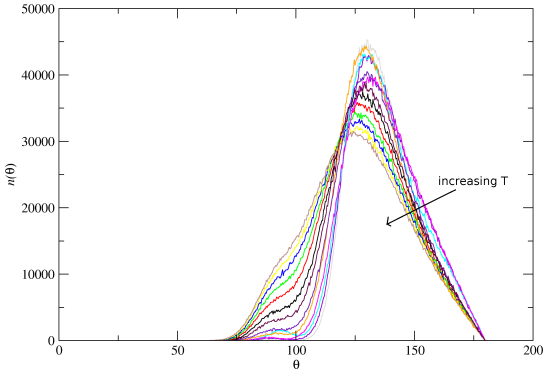

Figure 3.10: BAD for $\alpha = 10$ a.u.

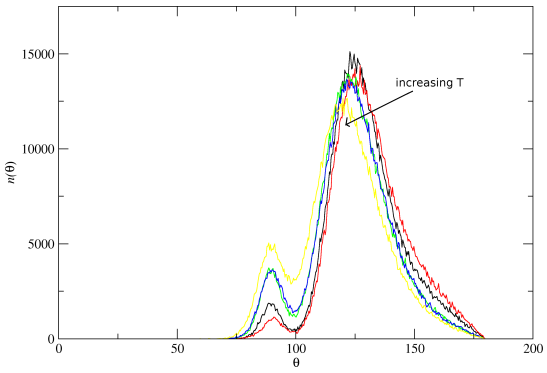

Figure 3.11: BAD for $\alpha = 15$ a.u.

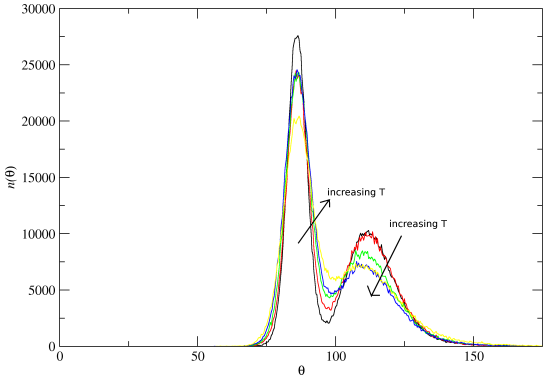

Figure 3.12: BAD for $\alpha = 20$ a.u.

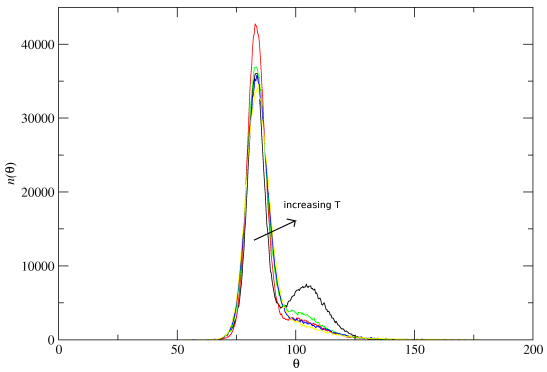

Figure 3.13: BAD for $\alpha = 25$ a.u.

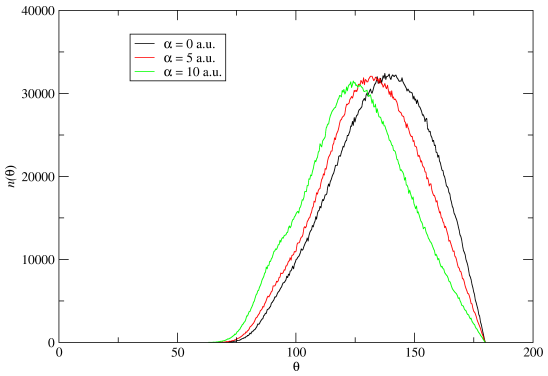

Figure 3.14: BAD for $T = 1500$ K

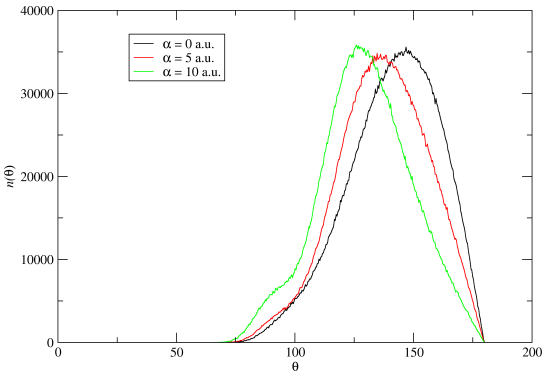

Figure 3.15: BAD for $T = 1100$ K

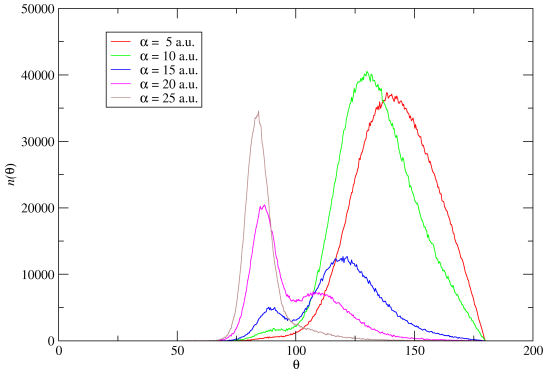

Figure 3.16: BAD for $T = 800$ K

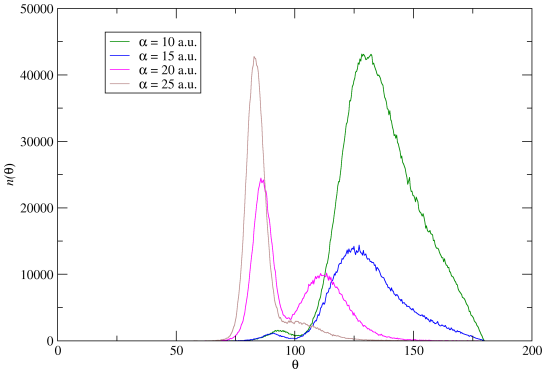

Figure 3.17: BAD for $T = 500$ K

4

Order Parameters

In order to study how structural or geometrical features of a liquid can be used to explain its anomalous thermodynamic and kinetic properties, we need a systematic method to quantify the order, or disorder, of a particular liquid. In this project, we follow the method introduced by Errington and Debenedetti in an attempt to explain "the relationship between structural order and the anomalies of liquid water" [15]. They define two types of order parameter: translational order parameter t, and orientational order parameter q. Whilst the translational order parameter is defined in order to investigate whether the ions in a liquid adopt a preferential separation, the orientational order parameter is defined in order to test how close the structure of a liquid is to perfect tetrahedral. In addition, they have observed how these variables are affected by temperature and density, and have studied how they are related in the order-parameter space.

4.1 Translational Order Parameter

4.1.1 Definition

The translational order parameter t, is defined by the following equation [43]:

$$t = \frac{\int_0^{\xi_c} |g_{ij}(\xi) - 1| \, \mathrm{d}\xi}{\xi_c}, \tag{4.1.1}$$

where $\xi = r\rho^{1/3}$ is the dimensionless distance, scaled by the mean separation between any two ions ($\rho^{-1/3}$) , $g_{ij}(\xi)$ is the radial distribution function (rdf) for

the ion pair ij, and ξ_c is a cut-off distance, which we choose to be 0.44 $N^{\frac{1}{3}}$, where N is the number density, so that it is consistent with the values used earlier by both Errington and Debenedetti [15] and Truskett *et al* [43]. The structure described in the previous chapters indicade that the structure of the cation sublattice is most susceptible to change. As a result, we define t in terms of the cation sublattice only, i.e., $i = j = \mathrm{M}^{2+}$.

The translational order parameter, defined in this manner, contains information about spatial separations of ions in a liquid; after all, the rdf measures the number density of particles from a reference particle, and the order parameter is an average value of rdf over the range $\xi \in [0, \xi_c]$. Note also that since all the atoms in an ideal gas are randomly distributed, its rdf is 1 for all r, and so $t = 0$, whereas for any system that is not completely disordered, the oscillations in the rdf leads to t being non-zero. In other words, t is zero for completely disordered systems and becomes non-zero for ordered systems.

4.1.2 Results and Discussion

The dependence of the translational order parameter on temperature is investigated first. Figure 4.1 and 4.2 show how the translational order parameter varies with temperature for systems at the polarisabilities of 0, 5, and 10 a.u., with fixed density at 4.0 and 5.4 g cm^{-3}, respectively. As temperature is increased, t decreases; this is reasonable for t measures how ordered the system is. Since the higher the temperature, the higher the average kinetic energy all the particles have, and the more disordered the system becomes, it is reasonable that t decreases as temperature is increased.

The dependence of the translational order parameter on anion polarisability is also captured in these two figures. Ignoring the case of very low temperature and high density, in which crystallisation may occur, it is clear that as anion polarisability is increased, t decreases. In Section 3.2, we found that as anion polarisability is increased, the number of edge-sharing units are increased. At the same time, the bond angle distribution becomes bimodal—there are acute-angle peaks and obtuse-angle peaks. Since there are two favourable configurations present in the systems with higher polarisabilities, e.g., $\alpha = 15$ a.u. (Figure 3.11),

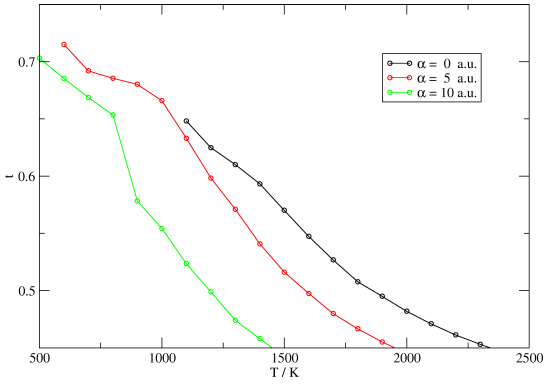

Figure 4.1: t for $\rho = 4.0$ g cm^{-3} ($\alpha = 0$, 5, 10 a.u.)

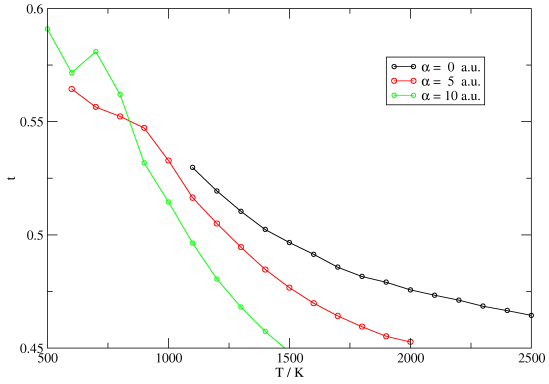

Figure 4.2: t for $\rho = 5.4$ g cm^{-3} ($\alpha = 0$, 5, 10 a.u.)

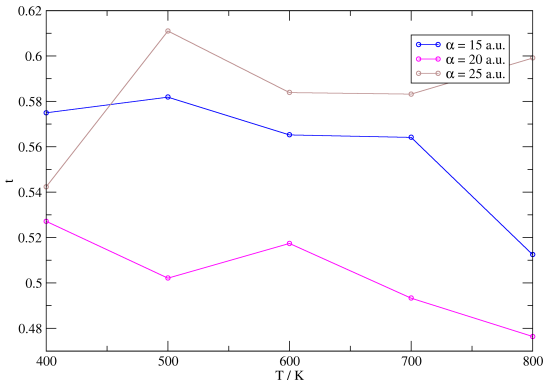

Figure 4.3: t for $\rho = 5.4$ g cm^{-3} ($\alpha = 15$, 20, 25 a.u.)

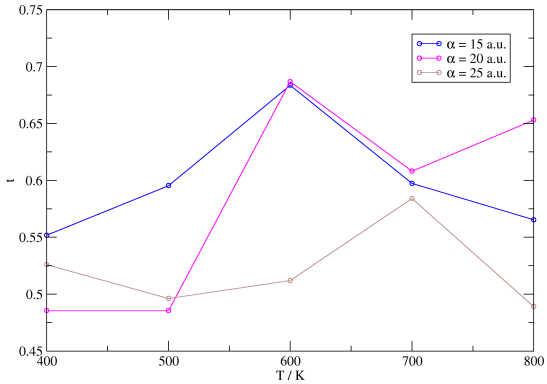

Figure 4.4: t for $\rho = 7.7$ g cm^{-3} ($\alpha = 15$, 20, 25 a.u.)

the system is less ordered. Therefore, the increase in polarisability yields systems with smaller values of translational order parameters.

Figure 4.3 and 4.4 show temperature dependence of the translational order parameters for systems kept fixed at the density of 5.4 and 7.7 g cm^{-3}, respectively, with higher values of polarisabilities and lower range of temperatures (Section 2.4.2). When the density is not extremely high, e.g., at 5.4 g cm^{-3} (Figure 4.3), t generally decreases as T is increased. However, when the density is very high, e.g, at 7.7 g cm^{-3} (Figure 4.4), that is no longer the case. It is plausible the system has either not reached the equilibrium—since T is low the simulation takes a long time to equilibrate—or has started to crystallise since T is low and ρ is high.

Since we are intending to work over a temperature range for which the system maybe supercooled, these results indicate that the translational order parameter may be useful for identifying crystallisation.

The translational order parameters from simulations performed at different temperatures (different colours in each figure) are plotted with respect to density, for fixed values of polarisability (Figures 4.5–4.10). It is clear that all the plots, both at different T and different α, have a few common features. The T-dependence of the translational order parameter is particularly clear—t decreases as temperature is increased, as expected—for simulations performed at low values of polarisability, $\alpha = 0$, 5, 10 a.u. (Figures 4.5–4.7). The values of t fluctuate more for simulations performed at higher polarisabilities, $\alpha = 15$, 20, 25 a.u., and lower temperatures (Figures 4.8–4.10). Regardless, t decreases as temperature is increased at low density. At higher density, there is a possibility that the systems may not have been at equilibrium and the data presented here is misleading. Since the tempertaure is low, which implies that particles have low kinetic energy, and the density is high, which means that particles are packed closely to each other, it is very likely that simulations need to be performed for longer time to achieve equilibrium.

At a fixed value of polarisability and temperature, the dependence of the translational order parameters on density is not as simple as that on temperature. Consider the results from simulations with no polarisability, $\alpha = 0$ a.u. (Figure 4.5). Whilst at high temperature (bottom curves: blue, dark green) t increases monotonically as density is increased, at low temperature (top curves: black and red) t increases until it reaches a maximum, decreases until it reaches a minimum, and eventually increases again. In general, if a system is compressed at constant T, since less space is available for particles to move, we expect the system to be more ordered. As a result, the systems appear to behave normally in high-temperature and high-density regime. We do, however, observe *anomalous* behaviour in intermediate density range, in which the system becomes less ordered (t decreases) upon compression; this implies that a directional short-range force, similar to the hydrogen bonds in water, is dominating the system.

Furthermore, it is clear from considering Figure 4.5–4.10 altogether that the locations of both the local maxima and minima depend critically on the anion

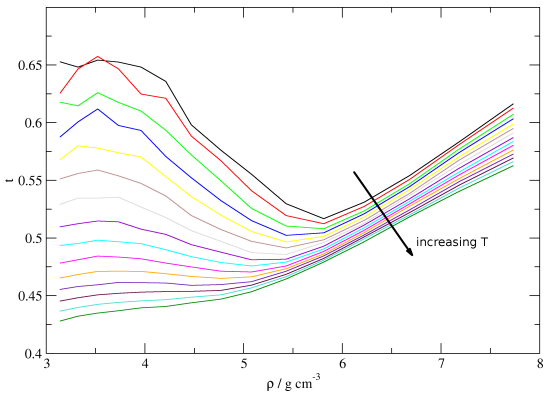

Figure 4.5: t for $\alpha = 0$ a.u.
Each line represents data at different temperatures, ranging from 1100 K (black) to 2500 K (dark green).

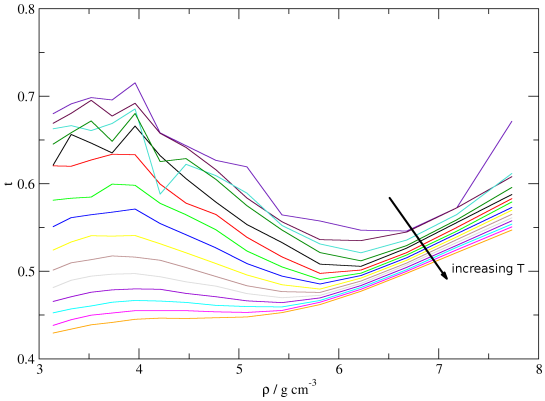

Figure 4.6: t for $\alpha = 5$ a.u.
T ranges from 600 K (indigo) to 2000 K (orange).

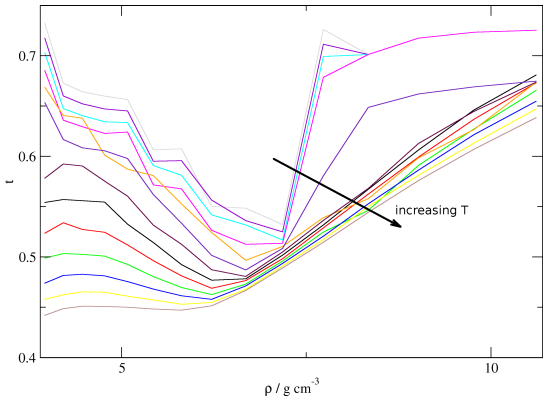

Figure 4.7: t for $\alpha = 10$ a.u.
T ranges from 300 K (grey) to 1500 K (brown).

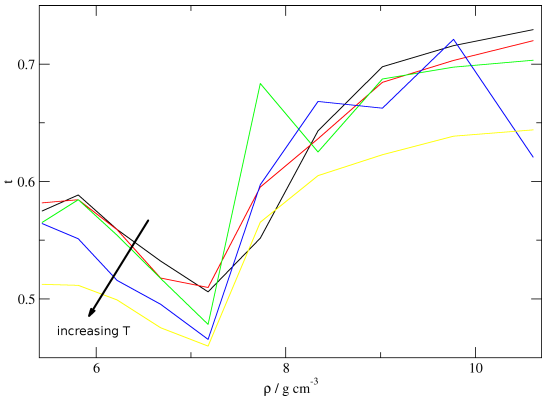

Figure 4.8: t for $\alpha = 15$ a.u.
T ranges from 400 K (black) to 800 K (yellow).

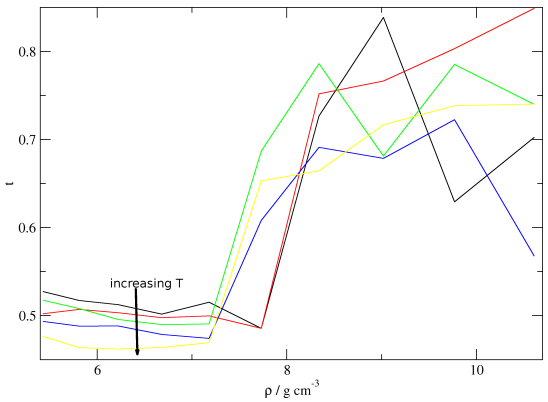

Figure 4.9: t for $\alpha = 20$ a.u.
The key is the same as in Figure 4.8.

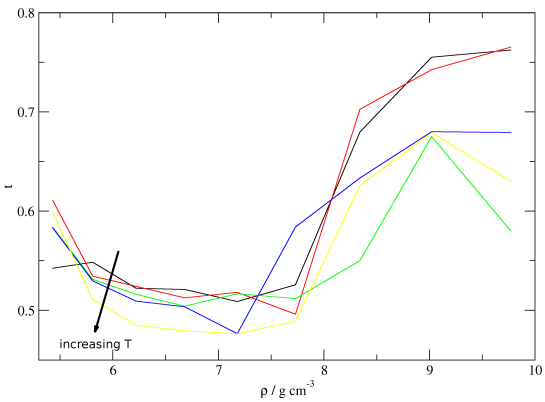

Figure 4.10: t for $\alpha = 25$ a.u.
The key is the same as in Figure 4.8.

polarisability. As anion polarisability is increased, both the maxima and minima move to higher density. For instance, at $T = 1500$ K, the maxima and minima occur approximately at the density of 3.5 and 5.5 g cm^{-3} (yellow line in Figure 4.5), 3.8 and 5.8 g cm^{-3} (brown line in Figure 4.6), and 4.5 and 6 g cm^{-3} (brown line in Figure 4.7), for simulations with $\alpha = 0$, 5, and 10 a.u., respectively. Finally, the temperature dependence of the location of the minima is less pronounced as anion polarisability is increased—whilst the minima for $\alpha = 0$ a.u. clearly move to lower density as T increased (Figure 4.5), the minima for higher α barely changes (Figure 4.8).

Since our ultimate goal is to capture the anomalous region of the network-forming systems based on different criteria, and investigate how the locations of these regions shift as polarisability is varied, we proceed to construct a line which separates out the anomalous region. The t-maxima are present at the low-density limit accessible to simulations and, as a result, are difficult to locate, or in some cases not present at all, for example, in the low-T region for $\alpha = 10$ a.u. (Figure 4.7). On the contrary, t-minima can be observed very clearly; thus, we use the line of t-minima as an upper boundary of the anomalous region. Figure 4.11 shows the location of these minima, plotted on the T–ρ plane, in the same manner as for the TMD lines (Figure 3.7). Only the t minima from simulations with $\alpha = 0$, 5, and 10 a.u. are given here; the t-minima lines for those with higher polarisability become vertical, i.e., t-minima occur practically at the same $\rho \approx 7.2$ g cm^{-3} for all T, and are not shown. These figures also emphasise how the line of t-minima shifts to higher-density and lower-temperature region as polarisability is increased, in the same manner as observed for the TMD lines (Figure 3.7), which implies that perhaps there is a correlation between the thermodynamic anomaly and this structural anomaly. Finally, although we only managed to construct the upper boundary of the structural anomalous region, the lower boundary will be created based on another structural criterion, the method of which is described and the lines constructed in the next section.

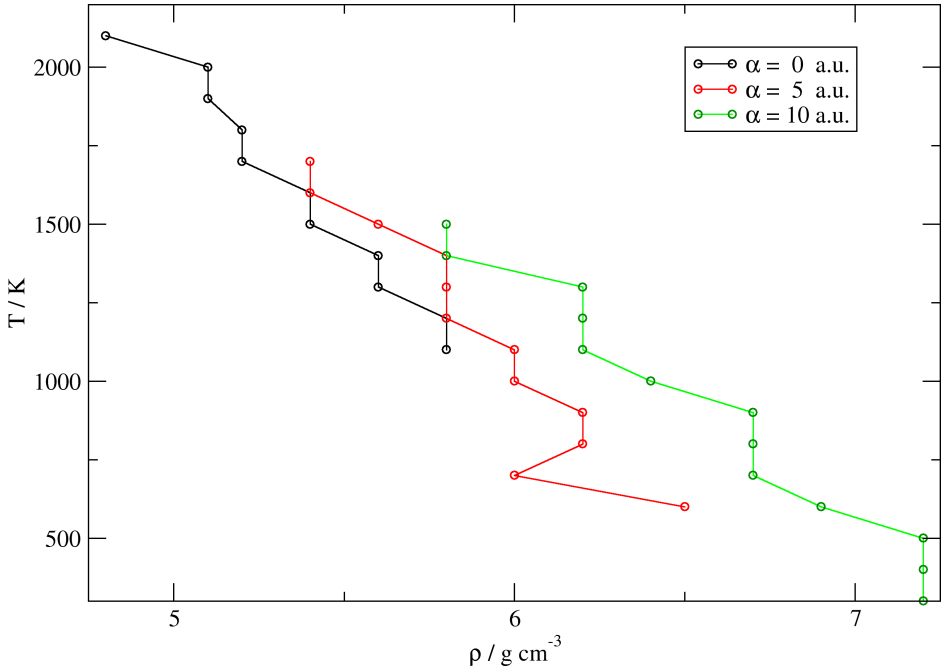

Figure 4.11: Lines of t-minima on T–ρ plane. Lines are shown for $\alpha = 0$ a.u. (black), 5 a.u. (red), and 10 a.u. (green).

4.2 Orientational Order Parameter

4.2.1 Definitions

The geometric study of liquid structure has been long investigated. It was pioneered by Bernal [4, 5], who suggested a parameter which would now be called a Voronoï tessellation [45]. Due to its complexity and computation time required, other simpler parameters have been proposed to quantify the structure of liquids. An example, of particular significance for the study of tetrahedral configurations, is the Q_l parameter, developed by Steinhardt *et al* [41], which is defined as

$$Q_l = \left[\frac{4\pi}{N(2l+1)} \sum_{m=-l}^{l} \left| \sum_{j=1}^{N} Y_l^m(\theta_j, \phi_j) \right|^2 \right]^{\frac{1}{2}}, \tag{4.2.1}$$

where N is the number of bonds, $Y_l^m(\theta_j, \phi_j)$ is the spherical harmonic, and θ_j and ϕ_j are the two polar angles of the jth bond with respect to the centre, and $1 \leq j \leq N$. Specifically, Q_3 measures how tetrahedral the structure is: $Q_3 = \frac{\sqrt{5}}{3}$

for perfect tetrahedral centre [11]. However, this value of Q_3 does not correspond uniquely to a tetrahedral environment—a certain type of pyramidal shape also corresponds to this value [12].

In this project, we follow Errington and Debenedetti [15], who use the modified definition of the Chau and Hardwick [12] orientational order parameter:

$$q = 1 - \frac{3}{8}\sum_{j=1}^{3}\sum_{k=j+1}^{4}\left(\cos\psi_{jk} + \frac{1}{3}\right)^2, \tag{4.2.2}$$

where ψ_{jk} is the angle at the central ion between j and k bonds. For perfect tetrahedron, $\psi_{jk} = 109.5°$, $\cos\psi_{jk} = -1/3$, and $q = 1$. On the other hand, for a totally random configuration (disordered system), the expectation of q is the value of q averaged over all possible angles on a unit sphere:

$$\langle q\rangle = \frac{\int\left[1 - \frac{3}{8}\sum_j{\sum_k}'\left(\cos\psi_{jk} + \frac{1}{3}\right)^2\right]\sin\psi_{jk}\,\mathrm{d}\psi_{jk}\,\mathrm{d}\phi}{\int\sin\psi\,\mathrm{d}\psi\,\mathrm{d}\phi} \tag{4.2.3}$$

$$= 1 - \frac{1}{2}\int_0^\pi \frac{3}{8}\cdot 6\left(\cos\psi + \frac{1}{3}\right)^2\sin\psi\,\mathrm{d}\psi \tag{4.2.4}$$

$$= 0. \tag{4.2.5}$$

The prime in the summation over the index k, in equation (4.2.3), is used to indicate that the sum is constrained and is carried out only for when $k > j$. In addition, in going from the equation (4.2.3) to equation (4.2.4), we have used the fact that since all angles are completely random, the summands are all equivalents and the double sum is reduced to a factor of 6, which is the number of different angles about a tetrahedral centre.

The modified definition of the orientational order parameter is chosen so that it is analogous to the definition of the translational order parameter: the order parameters are zero for a completely disordered system and are non-zero for ordered system, specifically, the orientational order parameter goes to unity for perfect tetrahedral centre.

4.2.2 Results and Discussion

Similar to the study of the translational order parameter, we first study how the orientational order parameter depends on temperature. Figure 4.12 and 4.13

show the dependence of q on temperature for systems with fixed density at 4.0 and 5.4 g cm^{-3}, respectively. Once again, for the same reason, q decreases as temperature is increased (Compare Figure 4.12 to Figure 4.1).

The dependence on the anion polarisability can also be inferred from these figures. Clearly, for fixed temperature and density, q decreases as anion polarisability is increased. As discussed in Section 4.1.2, when anion polarisability is increased, the bond angle distribution becomes bimodal and the system is less ordered. Therefore, we observe the expected decrease in the magnitude of the orientational order parameter as anion polarisability is increased.

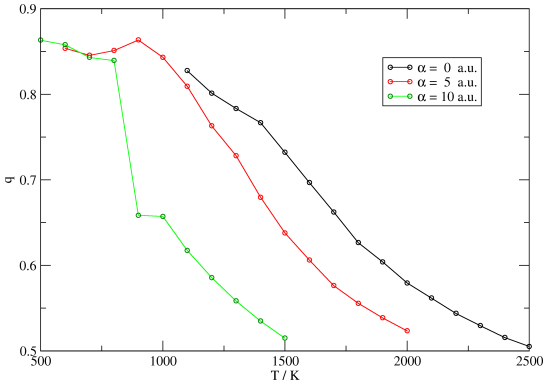

Figure 4.12: q for $\rho = 4.0$ g cm^{-3} ($\alpha = 0$, 5, 10 a.u.)

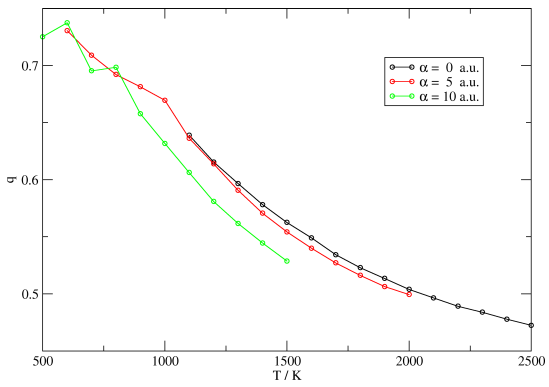

Figure 4.13: q for $\rho = 5.4$ g cm^{-3} ($\alpha = 0$, 5, 10 a.u.)

The dependence of q on density is shown in Figures 4.14–4.17. q indeed decreases when temperature is increased. However, the behaviour of the system at high-density region, including the anomalous behaviour, is different from that of t; for instance, compare Figure 4.14 to Figure 4.5. In the low-density region, increasing density leads to an increase in orientational order, for the same reason explained previously: increasing density leads to less space available for the particles in the system to move, and the system becomes more ordered. However, when then density is sufficiently high, further compression leads to a decrease in the tetrahedral orientational order. The orientational order parameter used in this study specifically measures how tetrahedral the system is; extreme compression may lead to other favourable configurations that are not tetrahedral. Therefore, though translational order is increased upon further compression, the

orientational tetrahedral order is not. As a result, instead of observing both local maxima and minima, as present in $t - \rho$ plots (for instance, Figure 4.5), only local maxima are observed.

As discussed earlier, we expect a system to be more ordered upon compression. Therefore, the local maxima of the q–ρ plots mark the lower boundary of the anomalous region. The plot of q-maxima against density (Figure 4.18) is constructed in the same manner as in the plot of t minima (Figure 4.11). Only the q maxima from simulations with $\alpha = 0$ and 5 a.u. are given here; the q-maxima lines for those with $\alpha = 10$ a.u., for instance, become vertical at $\rho \approx 4.6$ g cm^{-3}. Similar to other anomalous properties, the maxima line moves to higher-density and lower-temperature as polarisability is increased.

Finally, we plot both the lines of t minima (Figure 4.11), which indicate the upper bound of the anomalous region, and those of q maxima (Figure 4.18), which indicate the lower bound of the anomalous region onto the same $T - \rho$ plane (Figure 4.19). The region enclosed by the order parameter extrema curves are therefore the region in which the liquids exhibit anomalous behaviour. We shall compare this region to regions of other anomalous properties in the later chapter (Chapter 7).

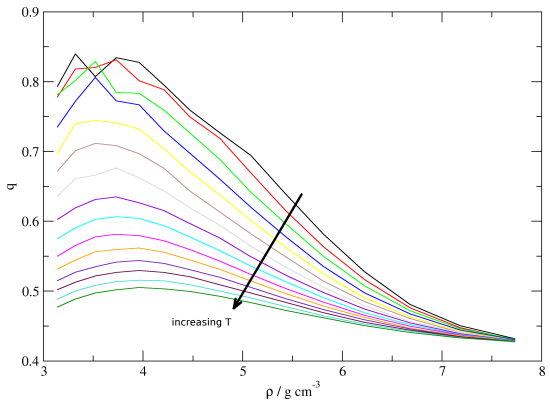

Figure 4.14: q for $\alpha = 0$ a.u.
Each line represents data at different temperatures, ranging from 1100 K (black) to 2500 K (dark green).

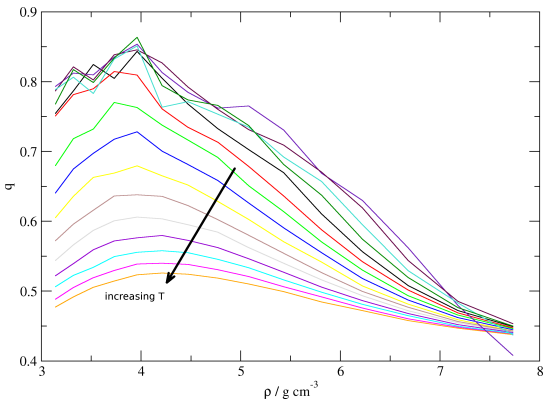

Figure 4.15: q for $\alpha = 5$ a.u.
T ranges from 600 K (indigo) to 2000 K (orange).

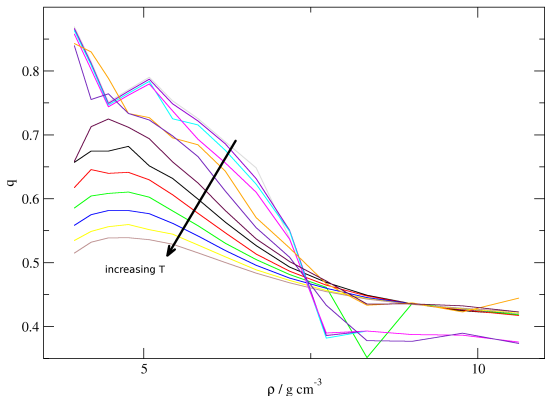

Figure 4.16: q for $\alpha = 10$ a.u.
T ranges from 300 K (grey) to 1500 K (brown).

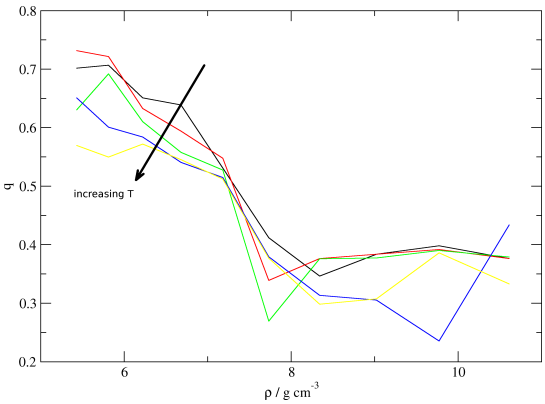

Figure 4.17: q for $\alpha = 15$ a.u.
T ranges from 400 K (black) to 800 K (yellow).

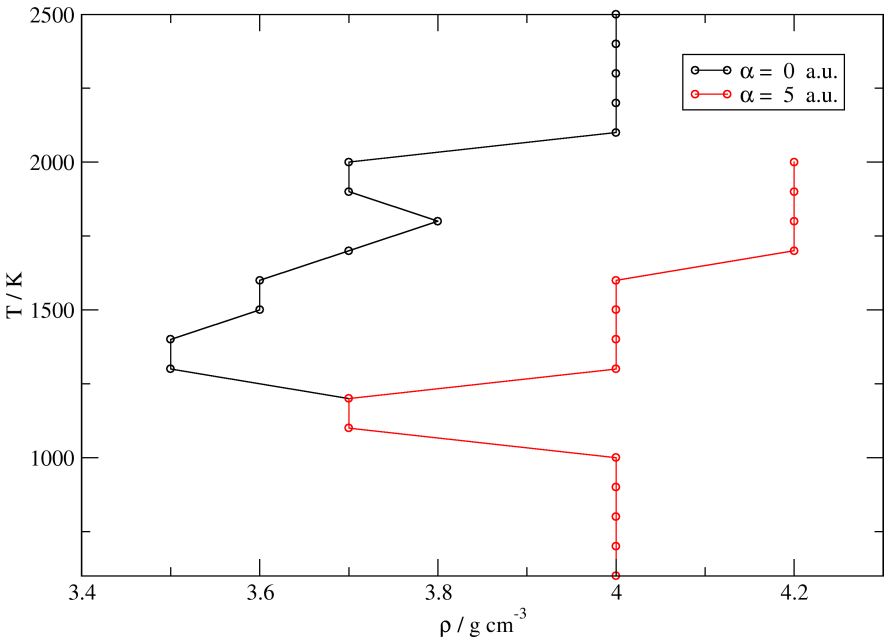

Figure 4.18: Lines of q-maxima on T–ρ plane. The key is as in Figure 4.11.

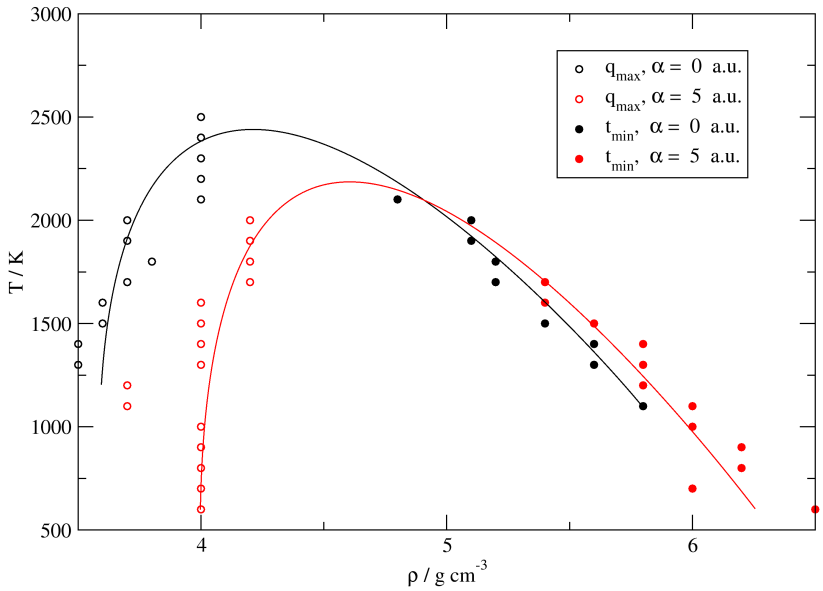

Figure 4.19: Regions of anomalous structural order for systems with $\alpha = 0$ a.u. (black) and 5 a.u. (red). Each region is bounded by the lines of order parameter extrema, of which we choose the the lower bound to be the line of q-maxima (empty circles) and the upper bound to be the line of t-minima (filled circles).

5

Diffusion

In the previous chapter, we have considered how static structural anomalous properties, in the form of translational and orientational order parameters, depend on the conditions of the system. In order to relate the structural order to the dynamic properties, the diffusion coefficients of the cations and anions are calculated. We shall see how they are related to order/disorder and also, like the preceding chapters, how they vary with temperature, pressure, density, and polarisability. In this chapter, the phenomenon of diffusion and related equations are briefly reviewed, followed by calculations of mean squared displacements and diffusion coefficients from molecular dynamics simulations. Finally, anomalies are highlighted.

5.1 Fick's Law and Diffusion Equation

A phenominological equation used to describe diffusion is known as Fick's law[10]:

$$\mathbf{j} = -D\,\nabla\rho, \tag{5.1.1}$$

where $\mathbf{j}$ is the particle current density, D is the diffusion coefficient, and ρ is the number density. The motivation for the equation is now discussed briefly. At equilibrium, particles suspended in a fluid are uniformly distributed. If the particles are moved or segregated somewhere by some external forces, which are later turned off, then the particle distribution must change in such a way that it eventually approaches the uniform equilibrium state. Thus, it is expected that

the driving force of diffusion is the concentration gradient, resulting in Fick's law, which states that the flux of particles, or the rate of flow of particles per unit area, is proportional to the concentration gradient.

In transport processes, particles do not multiply or disappear, i.e., the number of particles or the number density is conserved and does not vary with time, both globally and locally. The latter statement can be expressed as

$$\nabla \cdot \mathbf{j} = -\frac{\partial \rho}{\partial t}. \tag{5.1.2}$$

The literal interpretation of the expression is that the flux of particles that flow out of a point in space, the divergence, is equal to the decreasing rate (the minus sign) of the particle density of that same point.

By substituting Fick's law (5.1.1) into the particle conservation law (5.1.2), a differential equation, known as the diffusion equation, is obtained:

$$\frac{\partial \rho}{\partial t} = D\,\nabla^2 \rho. \tag{5.1.3}$$

The diffusion equation (5.1.3), subjected to the initial condition,

$$\rho(\mathbf{r}, 0) = N\,\delta(\mathbf{r}), \tag{5.1.4}$$

where N is the total number of particles, which implies that at $t = 0$ all particles are located at the origin, can be solved to give[1]:

$$\rho(\mathbf{r}, t) = \frac{N}{(4\pi D t)^{3/2}} e^{-|\mathbf{r}|^2/4Dt}. \tag{5.1.5}$$

This solution implies that the particles, initially accumulated at the origin, will spread out in time, with the mean-square radius being the value of the variance of the above Gaussian function:

$$\left\langle |\mathbf{r} - \mathbf{r}_0|^2 \right\rangle = \left\langle |\mathbf{r}|^2 \right\rangle = 6\,D\,t. \tag{5.1.6}$$

According to equation (5.1.6), the diffusion coefficient measures how fast mean-square displacement of the particles change linearly over time. Therefore, to evaluate the diffusion coefficient, we need to calculate the mean squared displacement of the particles.

[1]Refer to section 17-2 of [25] for full derivation.

5.2 Mean Squared Displacement Calculations

Since positions of all particles at every time step are recorded in molecular dynamics simulations, it is straightforward to calculate the displacement of the particle i at each time step: $\mathbf{r}_i(t) - \mathbf{r}_i(0)$. To find the mean-square displacement as a function of time, we have to average the square of the displacements over all particles at each time step t:

$$\left\langle |\mathbf{r}(t) - \mathbf{r}(0)|^2 \right\rangle = \frac{1}{N} \sum_{i}^{N} |\mathbf{r}_i(t) - \mathbf{r}_i(0)|^2, \tag{5.2.1}$$

where $0 \leq t \leq N_t \cdot \Delta t$, N_t is the total number of MD cycles performed, Δt is the universal time step increment, and N is the total number of particles.

However, once the system is in equilibrium, the initial position of a particle used as a reference for the displacement is arbitrary and can be chosen to be any point. Therefore, we could as well calculate the values of the mean-square displacements as a function of time, from an arbitrary initial position:

$$\left\langle |\mathbf{r}(t) - \mathbf{r}(t_0)|^2 \right\rangle = \frac{1}{N} \sum_{i}^{N} |\mathbf{r}_i(t) - \mathbf{r}_i(t_0)|^2, \tag{5.2.2}$$

where $0 \leq t_0 < N_t \cdot \Delta t$, and $t_0 \leq t \leq N_t \cdot \Delta t$. Note that the number of data points is N_t when $t_0 = 0$, and 1 when $t_0 = (N_t - 1)\Delta t$.

Since the error in an estimation of a statistical quantity is minimised as more data points are used, it is useful to also include the mean-square displacements from any arbitrary initial points in the calculation as well. Therefore, the mean-square displacement calculated in this study follows from the following equation:

$$\left\langle |\mathbf{r} - \mathbf{r}_0|^2 \right\rangle = \frac{1}{N_t + \cdots + 1} \sum_{j=0}^{N_t - 1} \left\langle |\mathbf{r}(t) - \mathbf{r}(j \cdot \Delta t)|^2 \right\rangle \tag{5.2.3}$$

$$= \frac{1}{\frac{1}{2} N_t (N_t + 1)} \sum_{j=0}^{N_t - 1} \left\langle |\mathbf{r}(t) - \mathbf{r}(j \cdot \Delta t)|^2 \right\rangle \tag{5.2.4}$$

$$= \frac{2}{N_t (N_t + 1)} \cdot \frac{1}{N} \sum_{j=0}^{N_t - 1} \sum_{i}^{N} |\mathbf{r}_i(t) - \mathbf{r}_i(j \cdot \Delta t)|^2. \tag{5.2.5}$$

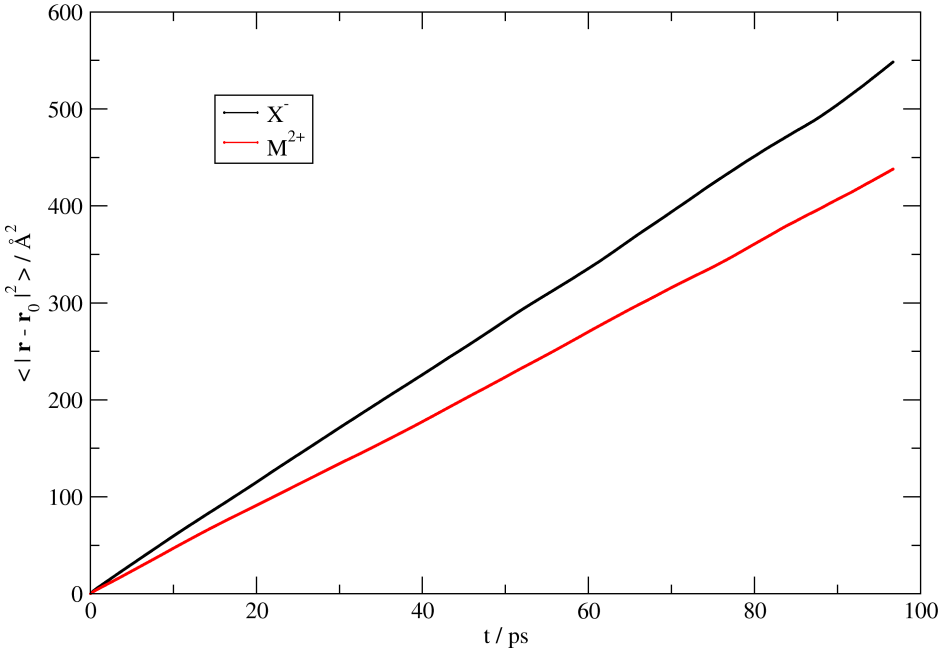

Figure 5.1: Mean squared displacement as a function of time for both the anion (black) and the cation (red) for RIM, $\alpha = 0$ a.u., for $\rho = 5.4$ g cm^{-3}, at $T = 2000$ K. The gradients are found to be 58.4×10^{-5} cm^2 s^{-1} and 42.8×10^{-5} cm^2 s^{-1}, which correspond to the values of the diffusion coefficient of 9.73×10^{-5} cm^2 s^{-1} and 7.14×10^{-5} cm^2 s^{-1} for the anion and the cation, respectively.

Figure 5.1 shows how the mean squared displacements of both the anion and the cation depend on time for RIM with the density of 5.4 g cm^{-3} at 2000 K. The equation (5.1.6) is satisfied as the plots are linear. Using the equation (5.1.6), the diffusion coefficient is a sixth of the gradient of the plot, which turns out to be 9.73×10^{-5} cm^2 s^{-1} for the anion and 7.14×10^{-5} cm^2 s^{-1} for the cation.

5.3 Results and Discussion

We begin by observing how the diffusion coefficients depend on temperature. Figure 5.2 shows how the diffusion coefficient of the anion (D_{X^-}) depends on temperature for three different values of anion polarisability, $\alpha = 0$, 5, 10 a.u. It is clear that the magnitude of the diffusion coefficient of the anions increases as the temperature increases. The dependence on temperature is trivial: when

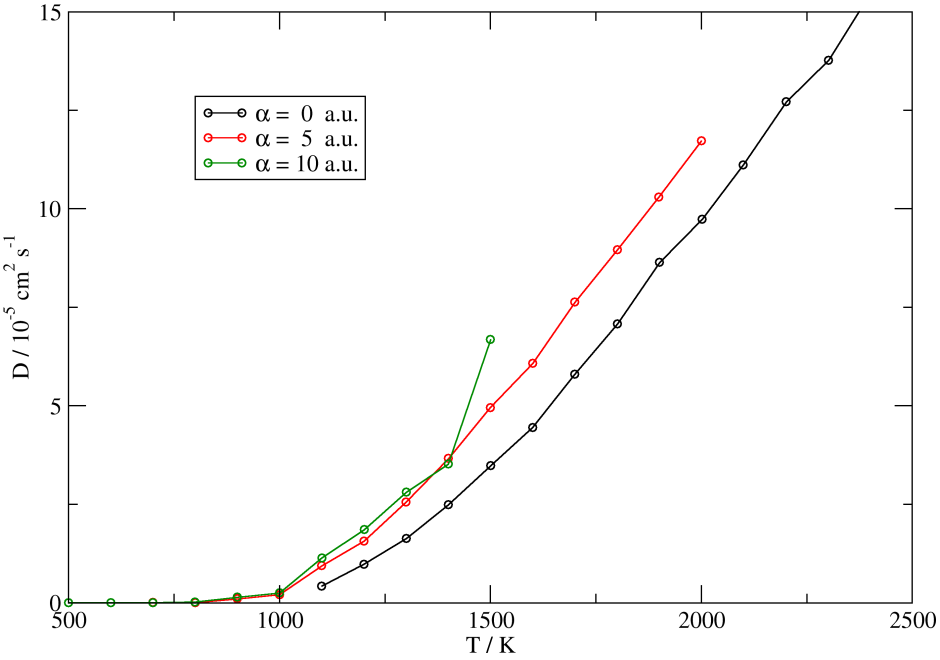

Figure 5.2: Diffusion coefficient for the anion D_{X^-}, for systems with fixed density of 5.4 g cm^{-3}, at three different values of polarisability, as a function of T. The key is as for Figure 3.6 with the additional green line for $\alpha = 10$ a.u.

temperature is increased, the ions have higher average kinetic energy; therefore, they move faster and the system possess higher value of diffusion coefficient. In addition, as anion polarisability is increased, at fixed temperature, the diffusion coefficient of the anion increases as well. Since increasing polarisability implies that the magnitude of the M–X–M angle is decreased (Section 3.2), i.e., the M–X–M bond is bent more, the anion may now diffuse past the cation without having to clash onto it (as in the extreme case of linear X–M–X). Alternatively, if one assumes a more cooperative motion of counterions, the inclusion of anion polarisability effectively softens the vibrational modes and reduces the heights of the activation barrier to collision on the energy landscape.

The diffusion coefficients of the cation ($D_{M^{2+}}$) have also been calculated. Figure 5.3 and 5.4 comparatively show the examples of diffusion coefficients of both the anion and the cation for two values of polarisabity, $\alpha = 0$ and 10 a.u. Not surprisingly, for the reason mentioned previously, diffusion coefficients of both the anion and the cation increase as temperature is increased. It is also obvious that

the values of diffusion coefficients of both species increase when polarisability is increased. (For instance, at $T = 1500$ K, whilst D of both species are approximately 3×10^{-5}cm^2 s^{-1} when $\alpha = 0$ a.u., the values are certainly greater than 5×10^{-5}cm^2 s^{-1} when α is increased to 10 a.u.) Furthermore, we have observed that the diffusion coefficients of the anion are larger than those of the cation. It is generally difficult to predict the relative magnitudes of diffusion coefficients of the two species as D depends on both the mass of the ions and the collision diameter. In this case, clearly, the effect of the mass predominates as the mass of the anion, which we take it to be that of Cl (35.5 g/mol), is about two times lighter than that of the cation, which we take the value of Zn (65.4 g/mol).

Furthermore, according to Figure 5.3 and 5.4, the dependence on both temperature and polarisability of the diffusion coefficients of both the anion and cation are almost the same, the only one exception being the diffusion coefficients of the anion are larger. Hence, from here onwards, we focus only on the behaviour of the anion.

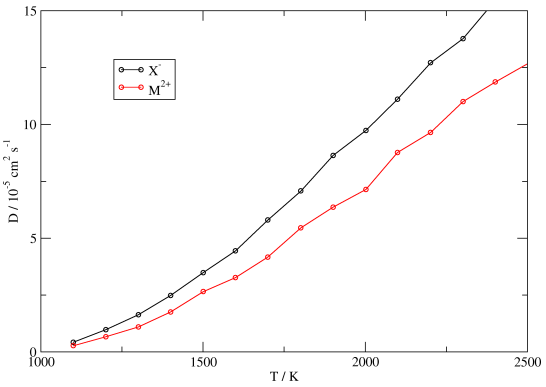

Figure 5.3: D of both the anion and the cation for the system with $\alpha = 0$ a.u. and density of 5.4 g cm^{-3}.

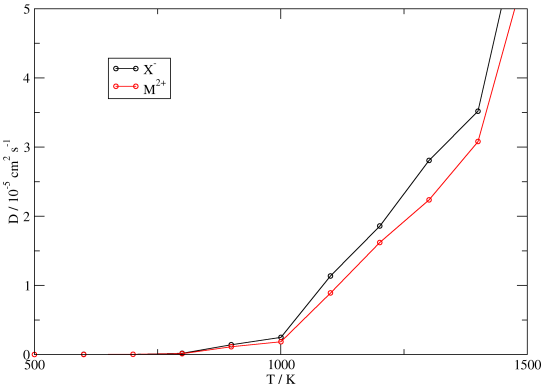

Figure 5.4: D of both the anion and the cation for the system with $\alpha = 10$ a.u. and density of 5.4 g cm^{-3}.

We shall now investigate the dependence of the diffusion coefficient on density. Figure 5.5 and 5.6 show how diffusion coefficients depend on density at the fixed polarisabilities of 0 and 5 a.u. As was previously discussed, the two figures clearly show that the diffusion coefficients increase when temperature is increased. The dependence on polarisability is difficult to see as the temperature range for the

two sets of simulations are different. Whilst the highest temperature at which simulations are performed is 2500 K for RIM ($\alpha = 0$ a.u.), it is 2000 K $\alpha = 5$ a.u. Therefore, if we consider the values at $T = 2000$ K and $\rho = 5$ g cm^{-3}, $D \approx 10 \times 10^{-5}$cm^2 s^{-1} for RIM (The sixth line from the top, magenta, in Figure 5.5) which is less than that of $\alpha = 5$ a.u., in which case $D = 12.5 \times 10^{-5}$cm^2 s^{-1} (The top line, green, in Figure 5.6). Similar to both pressure (Section 3.1) and order parameters (Chapter 4), the dependence of the diffusion coefficient on density is more complicated. As a general consideration, if a system is compressed, the density of the system is increased. It is more difficult for the particles to move as there is less space available for them. Therefore, the diffusion coefficient is expected to decrease as the density is increased. Such a behaviour is indeed observed either when temperature is sufficiently high, or at extreme densities. Clearly, we have also observed *anomalous* behaviour, in which case the diffusion coefficient *increases* as a system is compressed, in the intermediate-density regime. This region is bounded by diffusion coefficient maxima and minima.

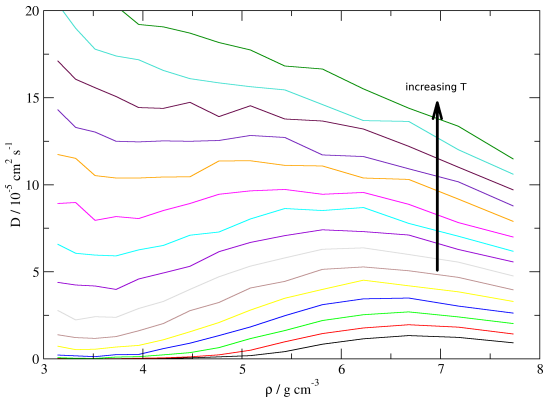

Figure 5.5: D for $\alpha = 0$ a.u. Each line represents data at different temperatures, ranging from 1100 K (black) to 2500 K (dark green).

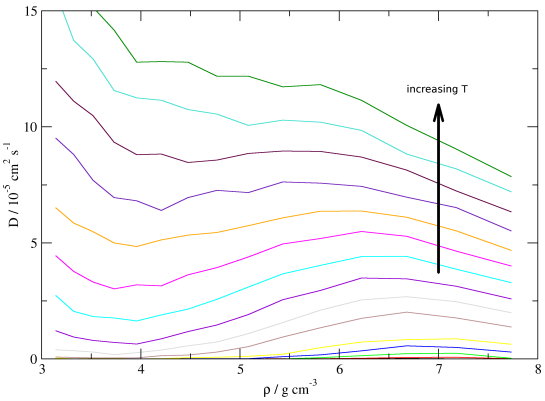

Figure 5.6: D for $\alpha = 5$ a.u. T ranges from 600 K (black) to 2000 K (dark green).

In order to locate this anomalous region, therefore, we plot both the D-minima and D-maxima of the D–ρ curves, at different temperature into a single T–ρ plane. Figure 5.7 shows the anomalous region for RIM and $\alpha = 5$ a.u.; as α is as large as 10 a.u., the line of $D_{\max}$ becomes almost vertical at $\rho \approx 6.7$ g cm^{-3}

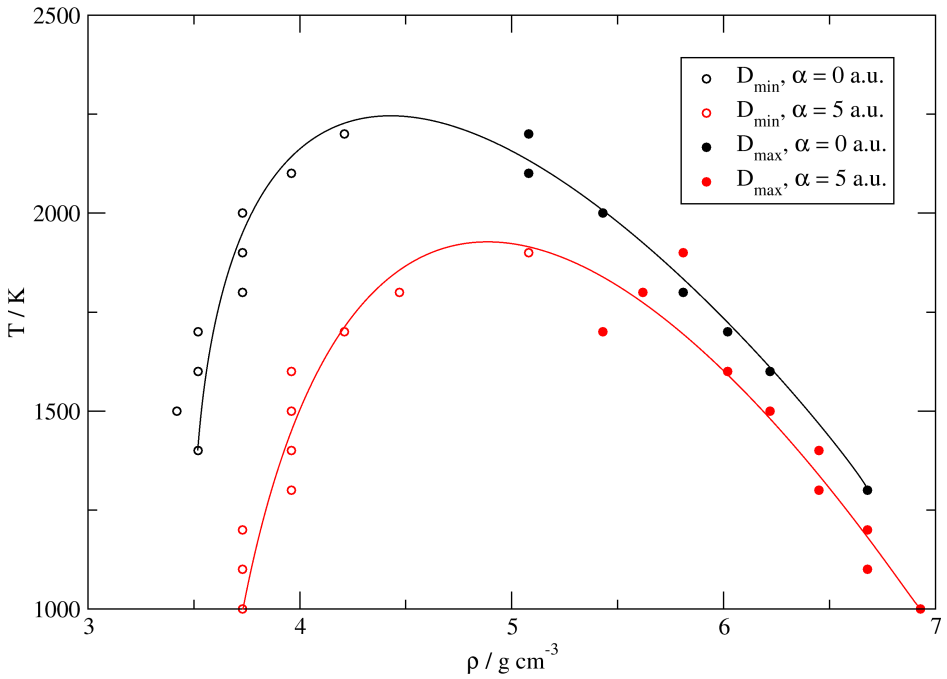

Figure 5.7: Regions of anomalous diffusivity for systems with $\alpha = 0$ a.u. (black line) and 5 a.u. (red line). Each region is bounded by the lines of diffusion coefficient extrema, of which the lower bound is the line of D-minima (empty circles) and the upper bound is the line of D-maxima (filled circles).

whilst D_{min} are rarely observed. The area enclosed by the curve is the anomalous region, i.e., the area in which diffusion coefficients are increased upon compression. Clearly, the anomalous region shifts to higher density and lower temperature as anion polarisability is increased.

6

Isothermal Compressibility

Another anomalous property of interest that is to be investigated in this chapter is the isothermal compressibility. In addition to the fact that we experimentally observe anomalies in isothermal compressibility, we also hope to use its behaviour as an evidence to support one of the thermodynamic scenarios, usually invoked to explain the anomalous behaviour of the supercooled water. We begin by presenting the definition of the isothermal compressibility. Since the motivation for studying the isothermal compressibility is to use it to support one of the thermodynamic scenarios, before the different methods of calculations are discussed in details, we explain the thermodynamic scenarios, two of which are traditional and involve singularties whilst the other is singularity-free. The main body of the chapter, outlining the calculations in details and presenting the results, then follows. Though unfortunately, we were unable to observe any anomalies in the isothermal compressibility from our simulations, we include the analysis in this chapter for completeness.

6.1 Definition

The isothermal compressibility, κ_T, is defined by the following equation:

$$\kappa_T = -\frac{1}{V}\left(\frac{\partial V}{\partial P}\right)_T. \tag{6.1.1}$$

It measures how easily a system can be compressed at fixed temperature. The minus sign is there to ensure the positivity of the quantity, as one would expect the system to be smaller—negative change in volume—upon applied pressure.

A few different approaches used to estimate the values of isothermal compressibility, besides directly calculated from the definition, are based on the following thermodynamic relation:

$$S_{\mathrm{NN}}(k \to 0) = \frac{\langle N^2 \rangle - \langle N \rangle^2}{\langle N \rangle} = \rho k_{\mathrm{B}} T \kappa_T, \tag{6.1.2}$$

where S_{NN} is the Bhatia–Thornton number–number structure factor, N is the number of atoms in the thermodynamic volume, $V \to \infty$, ρ is the number density, k_{B} is the Boltzmann constant, and κ_T is the isothermal compressibility. In general, we expect the value of the isothermal compressibility to increase as temperature is increased because we expect that the system becomes less dense and should be more compressible at high temperature.

6.2 Thermodynamics of Supercooled Water

Though we usually describe the origin of the anomalous properties of water as being a result of the increased hydrogen bonding between the water molecules as it is cooled down, the relationship between the macroscopic thermodynamic properties and the microscopic behaviour is not well established. Two thermodynamic scenarios, involving one or more critical points, and another singularity-free scenario, all of which invoke different thermodynamic mechanisms that explain the anomalous behaviour, have been proposed (Figure 6.1):

1. *Retracing spinodal scenario* (Figure 6.1a), proposed by Speedy [39, 40], suggests that the anomalous behaviour in the supercooled regime is due to the presence of a spinodal instability at low temperature, which causes the response functions to diverge as the temperature approaches the spinodal temperature. His analysis assumes that the slope of the TMD line stays negative at negative pressures. This scenario has not been experimentally verified since the nucleation of ice prevents the low-temperature measurements which may confirm the existence of the spinodal.

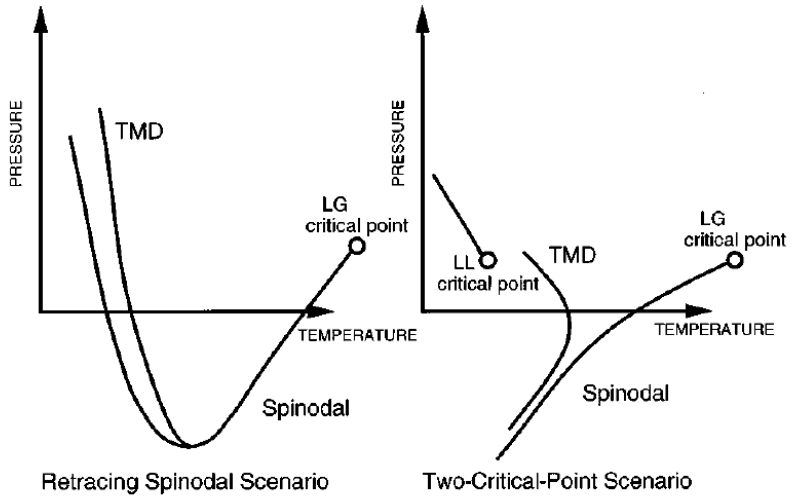

Figure 6.1: Schematic representation of the TMD line and the spinodal line in P–T plane for the two thermodynamic scenarios[2], both of which involve one or more critical points. (a) The retracing spinodal scenario, has only one liquid–gas (LG) critical point and the retracing spinodal line. (b) The two-critical-point scenario, includes the usual LG critical point and one addtional metastable liquid–liquid (LL) critical point. In the second scenario (b), the TMD line changes slope and is retracing whilst the spinodal does not.

2. *Critical-point scenario* (Figure 6.1b), proposed by Poole *et al.* [29, 30], suggests that the anomalous behaviour is due to the presence of an additional low-temperature liquid–liquid critical point, associated with the transition between a low-density and a high-density liquid phase. The suggestion is based on the computer simulations, in which they failed to observe the retracing spinodal whilst observing the inflection of the TMD line. There is a further experimental support of this scenario when first order transitions between low-density and high-density amorphous ice were observed [26, 27].

3. *Singularity-free scenario*, proposed by Sastry *et al.* [36], suggests that anomalous properties and any critical behaviour found in anomalous fluid

[2]The figure is reproduced from [36].

are totally independent. For instance, in this case, the anomaly in isothermal compressibility—decreasing in value upon heating—cannot be used to support any scenarios; both the anomaly and the retracing TMD arise as a result of thermodynamic requirements.

The three thermodynamic scenarios are distinct and our molecular dynamics simulation results can be used to support one of them. In the first two scenarios, it is clear that whilst the spinodal is retracing and intersects the TMD line in the first scenario, it is the TMD line that is retracing in the second scenario. In addition, there exists a region in which the slope of the TMD line is positive. Therefore, it is clear that results from our simulations did not support the retracing spinodal scenario as we observed the retracing TMD line (Figure 3.6).

Since the analysis of the behaviour of the isothermal compressibility plays a significant role in Sastry *et al*'s analysis, we shall investigate the isothermal compressibility of this network-forming material, and determine whether it follows the behaviour predicted: the slope of the TMD line changes sign when it intersects with the temperature of extremal compressibility.

6.3 Methods of Estimation

The values of the isothermal compressibility κ_T, may be estimated from the following quantities: the polynomial fit of $V(P)$, the number–number structure factor, and the number fluctuation. Whilst one of the methods is not particularly useful in our situation, two other methods that are used in this study are explained in details in this section.

6.3.1 Polynomial Fit of $P(V)$

Apparently, the isothermal compressibility can be directly estimated from the definition (6.1.1). By performing a polynomial fit of $P(V)$, we can calculate the isothermal compressibility using the reciprocal of the gradient of the polynomial. However, since the number of data points from each set of simulations is few, together with the fact that the pressure fluctuates very strongly in our systems (Figure 3.1–3.4), we choose to refrain from performing this method.

6.3.2 Number–Number Structure Factor

Bhatia and Thornton [6] defined three types of partial structure factors, which historically are useful for investigating the relationship between structures and electrical resistivity of binary alloys. They are extremely useful as the coherent scattering intensity, directly determined from a neutron diffraction experiment, can be expressed in terms of the three Bhatia–Thornton structure factors:

$$F(k) = \langle b \rangle^2 S_{\mathrm{NN}}(k) + (b_{\mathrm{M}} - b_{\mathrm{X}})^2 S_{\mathrm{CC}}(k) + 2 \langle b \rangle (b_{\mathrm{M}} - b_{\mathrm{X}}) S_{\mathrm{NC}}(k) - (c_{\mathrm{M}} b_{\mathrm{M}}^2 + c_{\mathrm{X}} b_{\mathrm{X}}^2), \tag{6.3.1}$$

where c_α and b_α are the atomic fraction and the coherent neutron scattering length of species α, respectively, and $\langle b \rangle = c_{\mathrm{M}} b_{\mathrm{M}} + c_{\mathrm{X}} b_{\mathrm{X}}$ is the weighted average of the neutron scattering lengths. $S_{\mathrm{NN}}(k)$ is the number–number structure factor, $S_{\mathrm{NC}}(k)$ is the number–concentration structure factor, and $S_{\mathrm{CC}}(k)$ is the concentration–concentration structure factor.

In practice, since we are working with molecular dynamics simulations, in which we know the positions of all particles in the system, it is usually more convenient to first calculate the partial pair distribution functions, $g_{\alpha\beta}(r)$. For homogenous single-component systems, the pair distribution function, $g(r)$ is defined through the following equation [18]:

$$\rho\, g(r) = \left\langle \frac{1}{N} \sum_i \sum_{j \neq i} \delta(\mathbf{r} - \mathbf{r}_j + \mathbf{r}_i) \right\rangle, \tag{6.3.2}$$

where ρ is the number density, N is the total number of particles, and $\mathbf{r}_i$ is the position of the particle i. This pair distribution function is interpreted as a probability of finding another particle at distance r from a reference particle, normalised in such a way that it tends to unity for large r. Alternatively, to be more precise, the quantity $\rho g(r) \cdot 4\pi r^2 \,\mathrm{d}r$ is the average number of particles lying between the distance of r and $r + \mathrm{d}r$ away from a reference particle. The peaks, therefore, represent shells of neighbours around the reference particle. The definition (6.3.2) can be generalised for multi-component systems:

$$c_\alpha\, c_\beta\, \rho\, g_{\alpha\beta}(r) = \left\langle \frac{1}{N} \sum_{i=1}^{N_\alpha} \sum_{\substack{j=1 \\ j \neq i}}^{N_\beta} \delta(\mathbf{r} - \mathbf{r}_j + \mathbf{r}_i) \right\rangle, \tag{6.3.3}$$

where c_α is the atomic fraction of species α, N_α is the number of species-α particles, and $N = N_\alpha + N_\beta$ is the total number of particles. This partial pair distribution function (Figure 6.2) now measures the probability of finding a species-α particle at a distance r away from a reference species-β particle.

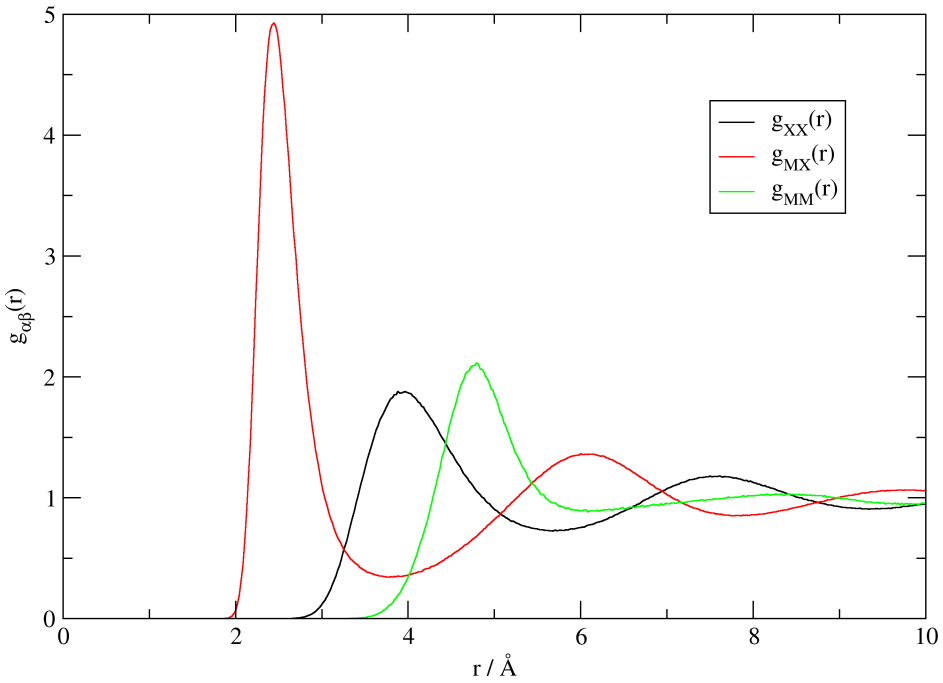

Figure 6.2: Partial pair distribution functions: $g_{\mathrm{XX}}(r)$ (black), $g_{\mathrm{MX}}(r)$ (red), and $g_{\mathrm{MM}}(r)$ (green). The results are obtained from a MD simulation with RIM ($\alpha = 0$ a.u.), at the density of 5.4 g cm^{-3} and the temperature of 2000 K.

According to Figure 6.2, the first peak appears approximately at 2.5 $\mathring{A}$, and this is of the $g_{\mathrm{MX}}(r)$ type, which implies that the adjacent layers of ions, of the sizes 2.5 $\mathring{A}$, are always between the cations and anions, which is to be expected as it is the interaction between cations and anions that stabilises ionic systems. Whilst the distance between the anionic layers is approximately 4 $\mathring{A}$, the distance between the cationic layers is almost 5 $\mathring{A}$. Since the charge of the cation is +2 whilst that of the anion is -1, we expect the ionic repulsion between the cations, hence the distance between them, to be greater than that of anions.

Once the partial pair distribution function, $g_{\alpha\beta}(r)$, is calculated, another type of structure factors, the Faber–Ziman partial structure factors, $S_{\alpha\beta}(k)$, can be

directly calculated as Fourier transforms of them [16]:

$$S_{\alpha\beta}(k) - 1 = \frac{4\pi\rho}{k} \int_0^\infty (g_{\alpha\beta}(r) - 1) \sin(kr)\, r\, \mathrm{d}r. \tag{6.3.4}$$

The Faber–Ziman partial structure factors (Figure 6.3) are quite useful as well since the experimental coherent scattering intensity can also be expressed in terms of these three partial structure factors:

$$F(k) = c_\mathrm{M}^2 b_\mathrm{M}^2 [S_\mathrm{MM}(k) - 1] + c_\mathrm{X}^2 b_\mathrm{X}^2 [S_\mathrm{XX}(k) - 1] + 2 c_\mathrm{M} c_\mathrm{X} b_\mathrm{M} b_\mathrm{X} [S_\mathrm{MX}(k) - 1]. \tag{6.3.5}$$

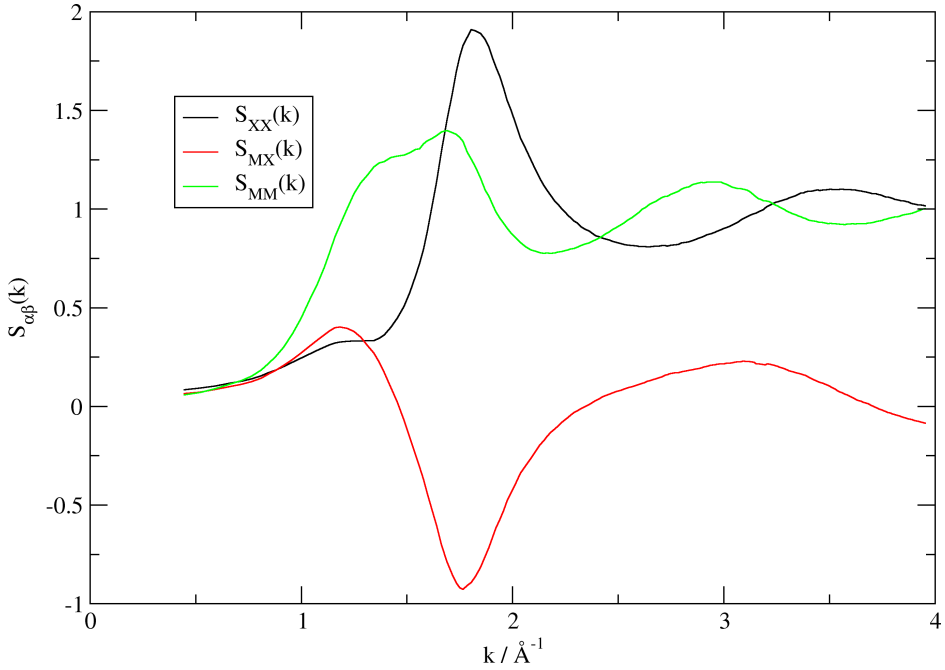

Figure 6.3: Faber–Ziman partial structure factors: $S_\mathrm{XX}(k)$ (black), $S_\mathrm{MX}(k)$ (red), and $S_\mathrm{MM}(k)$ (green). The results are obtained from the same MD simulation that is used to produce the partial pair distribution function in Figure 6.2.

Finally, the three Bhatia–Thornton partial structure factors, $S_\mathrm{NN}(k)$, $S_\mathrm{NC}(k)$, and $S_\mathrm{CC}(k)$, are then calculated from the Faber–Ziman partial structure factors, $S_{\alpha\beta}(k)$, by the following equations [33]:

$$S_\mathrm{NN}(k) = c_\mathrm{M}^2 S_\mathrm{MM}(k) + c_\mathrm{X}^2 S_\mathrm{XX}(k) + 2 c_\mathrm{M} c_\mathrm{X} S_\mathrm{MX}(k), \tag{6.3.6}$$

$$S_\mathrm{NC}(k) = c_\mathrm{M} c_\mathrm{X} \{ c_\mathrm{M} [S_\mathrm{MM}(k) - S_\mathrm{MX}(k)] - c_\mathrm{X} [S_\mathrm{XX}(k) - S_\mathrm{MX}(k)] \}, \tag{6.3.7}$$

$$S_\mathrm{CC}(k) = c_\mathrm{M} c_\mathrm{X} \{ 1 + c_\mathrm{M} c_\mathrm{X} [S_\mathrm{MM}(k) + S_\mathrm{XX}(k) - 2 S_\mathrm{MX}(k)] \}. \tag{6.3.8}$$

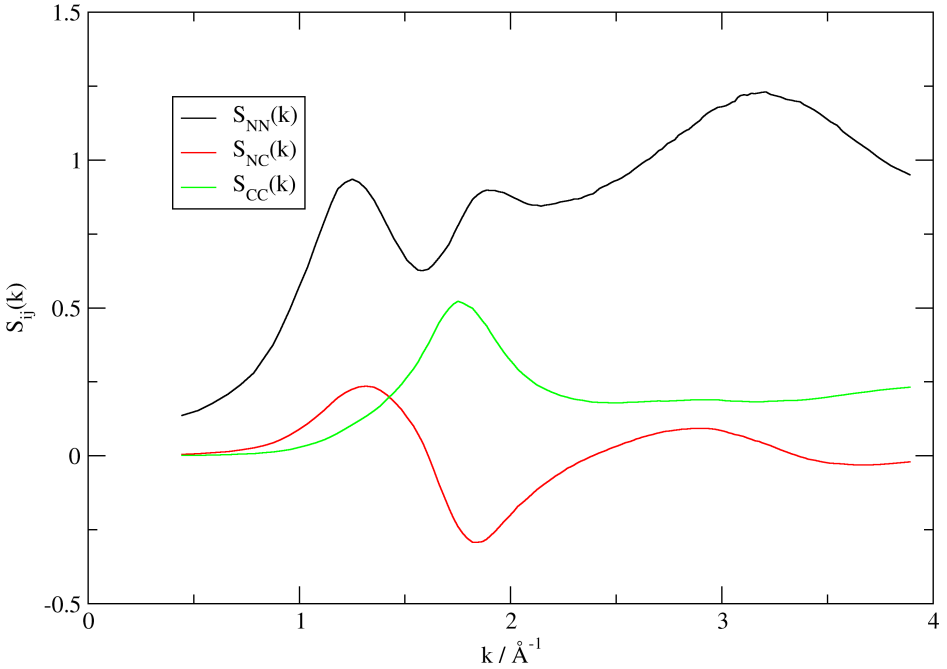

Figure 6.4: Bhatia–Thornton partial structure factors: $S_{\mathrm{NN}}(k)$ (black), $S_{\mathrm{NC}}(k)$ (red), and $S_{\mathrm{CC}}(k)$ (green). The results are obtained from the same MD simulation that is used to produce the partial pair distribution function in Figure 6.2.

$S_{\mathrm{NN}}(k)$ (the black line in Figure 6.4) is referred to as the Bhatia–Thornton number–number structure factor. Its Fourier transform describes the overall structure of the liquid without differentiating between particles of different species. Therefore, if the coherent neutron scattering length of the two species are equal, the equation (6.3.1) shows us that indeed the experimental coherent scattering intensity is directly proportional *only* to, this number–number structure factor.

$S_{\mathrm{NC}}(k)$ (the red line in Figure 6.4) is referred to as the Bhatia–Thornton number–concentration structure factor. Its Fourier transform describes the correlation between the sites and their occupancy by each species. If the two species are equivalent (ideal solution), $S_{\mathrm{NC}}(k) = 0$. Note, however, that it is possible that $S_{\mathrm{NC}}(k) = 0$ for some real 1:1 binary systems (MX), for instance, when the two species are of similar sizes and shapes and their environments are identical, specifically, when the mean coordination environment of M, $c_{\mathrm{M}}g_{\mathrm{MM}}(r)+c_{\mathrm{X}}g_{\mathrm{MX}}(r)$, is equal to that of X, $c_{\mathrm{X}}g_{\mathrm{XX}}(r) + c_{\mathrm{M}}g_{\mathrm{MX}}(r)$.

$S_{\mathrm{CC}}(k)$ (the green line in Figure 6.4) is referred to as the Bhatia–Thornton concentration–concentration structure factor. Its Fourier transform describes the ordering of the chemical species with respect to the sites specified by $S_{\mathrm{NN}}(k)$. If the two species are equivalent, $S_{\mathrm{CC}}(k)$ is constant.

Finally, these three Bhatia–Thornton structure factors are linked to the thermodynamic properties at $k = 0$. Specifically [6],

$$S_{\mathrm{NN}}(0) = \rho k_{\mathrm{B}} T \kappa_{\mathrm{T}} + \delta^2 S_{\mathrm{CC}}(0), \tag{6.3.9}$$

$$S_{\mathrm{NC}}(0) = -\delta S_{\mathrm{CC}}(0), \tag{6.3.10}$$

$$S_{\mathrm{CC}}(0) = N k_{\mathrm{B}} T / \left(\frac{\partial^2 G}{\partial c_{\mathrm{M}}^2} \right)_{T,P,N}, \tag{6.3.11}$$

where G is the Gibbs free energy, and $\delta = \rho(v_{\mathrm{M}} - v_{\mathrm{X}})$, with v_α being the partial molar volume per particle of species α, is the dilation factor, which is usually small for any solid solutions whose constituents are miscible in all proportions. Thus, the equation (6.3.9) indeed reduces to part of the equation (6.1.2). In addition, these three Bhatia–Thornton structure factors separate the correlations between the global non-crystalline structure ($S_{\mathrm{NN}}(k)$) from the chemical ordering ($S_{\mathrm{CC}}(k)$).

Salmon suggested that $S_{\mathrm{NN}}(k)$ can be expanded in terms of the running moments of $g_{NN}(r) - 1$, which is the Fourier transform of $S_{\mathrm{NN}}(k)$ itself, i.e.,

$$S_{\mathrm{NN}}(k) - 1 = \frac{4\pi\rho}{k} \int_0^\infty (g_{\mathrm{NN}}(r) - 1) \sin(kr)\, r \, \mathrm{d}r, \tag{6.3.12}$$

through the following equation [34]:

$$S_{\mathrm{NN}}(k) - 1 = M_{\mathrm{NN}}^{(0)} + M_{\mathrm{NN}}^{(2)} k^2 + M_{\mathrm{NN}}^{(4)} k^4 + ... \tag{6.3.13}$$

The running moments are defined as

$$M_{\mathrm{NN}}^{(2m)}(r_{\max}) = \int_0^{r_{\max}} \rho_{\mathrm{NN}}^{(2m)}(r)\, \mathrm{d}r, \tag{6.3.14}$$

and the weighted pair-distribution functions as

$$\rho_{\mathrm{NN}}^{(2m)}(r) = \frac{4\pi\rho(-1)^m}{(2m+1)!} (g_{\mathrm{NN}}(r) - 1) r^{2m+2}. \tag{6.3.15}$$

Since the equation (6.1.2) suggests that the isothermal compressibility κ_T, is related to the long-wavelength limit of $S_{\mathrm{NN}}(k \to 0)$, we may then estimate it by the expansion (6.3.13). Specifically, the terms of orders higher than k^2 are dropped, and $S_{\mathrm{NN}}(k)$ plotted against k^2. The y-intercept is therefore the long-wavelength limit $S_{\mathrm{NN}}(k \to 0)$.

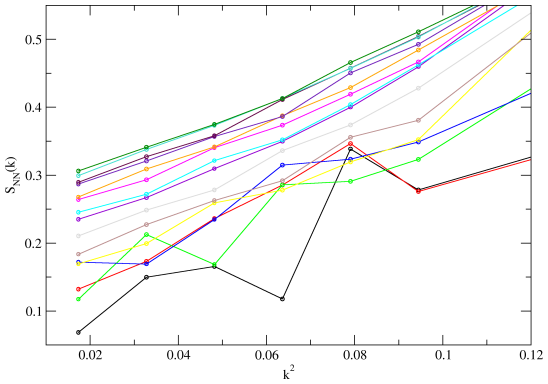

Figure 6.5: S_{NN} vs k^2 for $\rho = 4.0$ g cm^{-3}, $\alpha = 0$ a.u. The different lines correspond to different T, with T increasing from bottom to top.

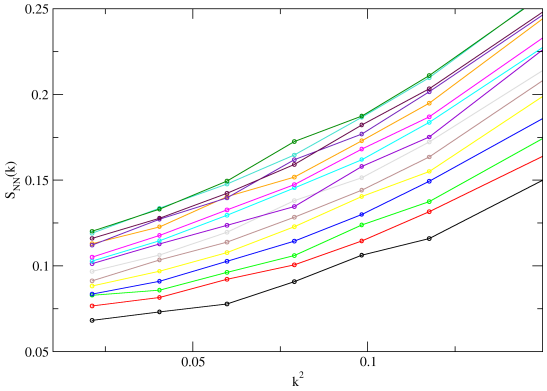

Figure 6.6: S_{NN} vs k^2 for $\rho = 5.4$ g cm^{-3}, $\alpha = 0$ a.u.

Figure 6.5 and 6.6 show the plots of S_{NN} vs k^2 at different temperatures. It is clear that the data sets from higher-density systems (Figure 6.6) presented here are somewhat linear. The data sets from lower-density systems (Figure 6.5) contain those that are linear (at hight T) and those that fluctuate strongly (at low T). In order to quantitatively determine the y-intercept and estimate the error bar, a linear regression is performed twice on each data set, once with 3 data points at lowest values of k, and the other with 6 data points. The reported values of the isothermal compressibility are the average between the two values. Since the error estimated by the linear regression method is usually smaller than the difference between the two calculated values, the error is taken to be the half range, or a half of the difference between the two values. Note that the coefficients of determination, R^2, calculated by the linear regression method is quite good. For instance, $R^2 \in [0.9536, 0.9997]$ for $\rho = 5.4$ g cm^{-3} and $R^2 \in [0.9195, 0.9982]$ for $\rho = 4.0$ g cm^{-3}, $T \geq 1500$ K (excluding the data sets at low T where strong fluctuation is clearly observed).

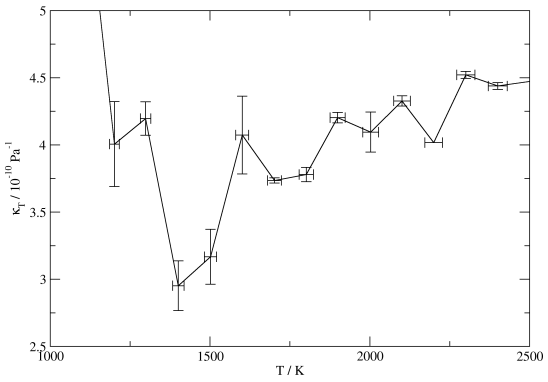

Figure 6.7: κ_T, calculated from S_{NN} for $\rho = 4.0$ g cm^{-3} and $\alpha = 0$ a.u. The MD simulation is performed for 200 000 cycles.

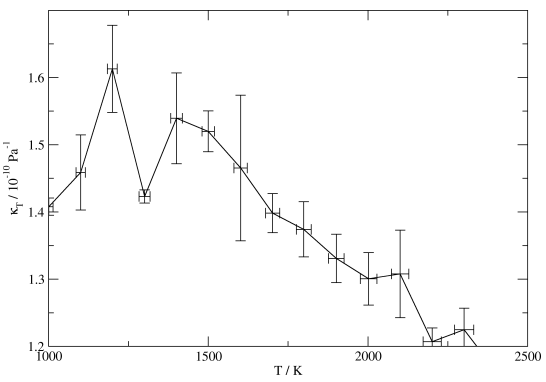

Figure 6.8: κ_T, calculated from S_{NN} for $\rho = 5.4$ g cm^{-3} and $\alpha = 0$ a.u. The MD simulation is performed for 200 000 cycles.

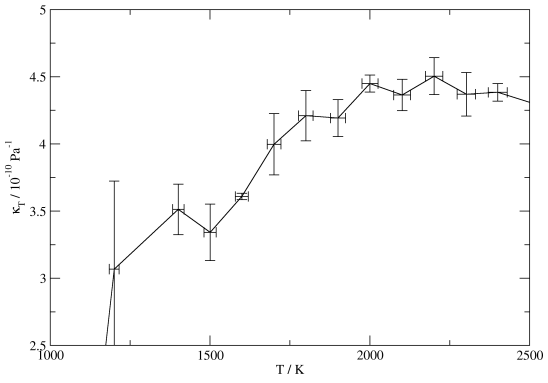

Figure 6.9: κ_T, calculated from S_{NN} for $\rho = 4.0$ g cm^{-3} and $\alpha = 0$ a.u. The MD simulation is performed for 3 000 000 cycles.

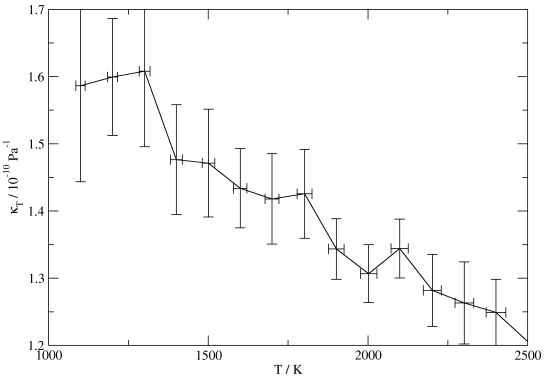

Figure 6.10: κ_T, calculated from S_{NN} for $\rho = 5.4$ g cm^{-3}and $\alpha = 0$ a.u. The MD simulation is performed for 3 000 000 cycles.

Figure 6.7 and 6.8 show how the isothermal compressibility, calculated for the RIM, $\alpha = 0$ a.u., at the same densities of 4.0 and 5.4 g cm^{-3}, respectively, depend on T. Despite the good linearity found earlier in plots of S_{NN} vs k^2 (Figure 6.5 and 6.6), the fluctuation in the data is very obvious—no clear trends are observed, suggesting that either the system is actually not yet at equilibrium or the finite-size effect [32] is too severe. (De Graff and Thorpe discussed the difficulty in calculating the isothermal compressibility from structure factors [13], though their systems contain 4 096 and 100 000 atoms, a much larger number than our 324.) This observation leads us to performing the second set of simulations running with 3 000 000 MD cycles, rather than the present 200 000 cycles, whose results are present in Figure 6.9 and 6.10.

Clearly, the results from the two sets of simulations, for instance, at the density of 4.0 g cm^{-}3 (Figure 6.7 and 6.9), significantly differ—one could have roughly guessed that a local minimum is present in Figure 6.7. However, the two sets of simulations possess the same behaviour in the high-temperature limit, which either suggests that at low temperature the simulations are either not yet in equilibrium or that this method of estimation is severely sensitive to the size of the system or the simulation time-scale.

6.3.3 Number Fluctuation

De Graff and Thorpe showed that an estimation of the isothermal compressibility from the structure factors may severely suffer from the finite-size effect, and a solution is to perform the estimation from the number fluctuation instead [13]. The authors suggest that the number fluctuation can be calculated by placing sampling spheres randomly into the system and count the number of particles in those spheres, then calculate the variance. Torquato and Stillinger [42] found the relationship between the number fluctuation and the size of the sampling sphere to be

$$\frac{\langle N(R)^2\rangle - \langle N(R)\rangle^2}{\langle N(R)\rangle} = 1 - \rho\frac{4\pi}{3}R^3 + \frac{1}{n}\sum_{i\neq j}^{n}\alpha(r;R), \tag{6.3.16}$$

where n is the total number of atoms in the system, and the function $\alpha(r;R)$ is the fractional intersection volume of the two spheres, with radii R, whose centres

are separated by the distance of r, and is given by

$$\alpha(r;R) = 1 - \frac{3}{4}\frac{r}{R} + \frac{1}{16}\left(\frac{r}{R}\right)^3 = \left(1 - \frac{r}{2R}\right)^2 \left(a + \frac{r}{4R}\right),\ r \leq 2R; \qquad (6.3.17)$$

and is zero if $r > 2R$.

De Graff and Thorpe then show that the relative fluctuation and the number–number structure factor are related only in the limit that $R \to \infty$ and $k \to 0$. Hence, by Taylor expanding the factor $\alpha(r;R)$ in intergral powers of $1/R$, the relative fluctuation may be written as

$$\frac{\langle N(R)^2\rangle - \langle N(R)\rangle^2}{\langle N(R)\rangle} = a + \frac{b}{R} + ... \qquad (6.3.18)$$

Therefore, the constant term is the long-wavelength limit of the structure factor.

In order to perform linear regression of the relative number fluctuation as a function of $1/R$, according to the method presented, the range of $1/R$ chosen should be such that the fluctuation is linear in $1/R$. The upper bound of $1/R$, or the minimum value of the radius of the sampling sphere, corresponds to the distance at which strong correlations in atom pair separations all but vanish. The lower bound of $1/R$ chosen, or the maximum value of the sampling sphere radius, corresponds to the maximum radius at which the finite size of the simulating system causes the fluctuation to start losing its linearity [13, 32].

According to our results, the relative fluctuation is linear when the radius of the sampling sphere used is between $R \in [\frac{L}{9}, \frac{L}{7}]$. Thus, we shall perform linear regression in such a region. Examples of the linear regression performed on various systems are shown in Figure 6.11 and 6.12; the results are obtained from the RIM MD simulations performed with the density of 4.0 and 5.4 g cm^{-3}, respectively.

Whilst most of the data sets presented here are linear, quite unfortunately, there is no obvious relationship between the y-intercept of these lines and the temperatures. In fact, it is found that many of the isothermal compressibilities calculated from this method, i.e., the y-intercept divided by the number density, the Boltzmann constant, and the temperature, followed from the equation (6.1.2), are negative. According to the method used by de Graff and Thorpe [13], the size of the sampling sphere R may not exceed $L/4$; otherwise, the sampling volume

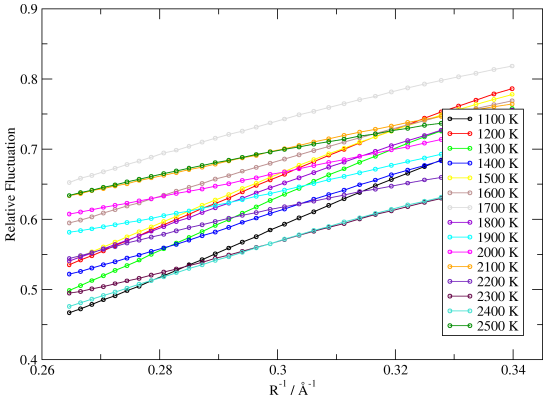

Figure 6.11: Relative Fluctuation for $\rho = 4.0$ g cm^{-3} and $\alpha = 0$ a.u.

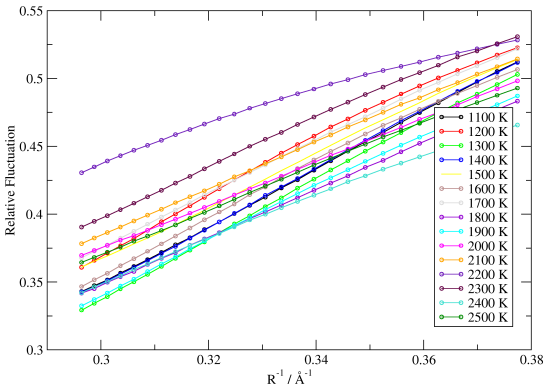

Figure 6.12: Relative Fluctuation for $\rho = 5.4$ g cm^{-3} and $\alpha = 0$ a.u.

factor $\alpha(r; R)$ is zero. Since de Graff and Thorpe performed the MD simulations in the cell, whose sides are 124 $\mathring{A}$ whilst ours are only up to 29 $\mathring{A}$, it is very possible that in our case, the size of the simulation cell is not large enough to allow us to extrapolate to the $1/R \to 0$ or $R \to \infty$ limit.

Though it is possible to increase the system size, the simulations require much more computational resources. Whilst it takes 6 days of actual run time to finish the 324-ion RIM simulations and 20 days for PIM, the 999-ion simulations comsume no fewer than 60 days for RIM. Surely, the PIM simulations require longer time of no fewer than 180 days for each simulation condition. We choose to not to pursue this direction of study and therefore neglect further discussion of the isothermal compressibility.

7

Cascade of Anomalies

In previous chapters, we have calculated the quantities important to the study of anomalous properties: pressure, temperature, translational and orientational order parameters, and diffusion coefficients. In this chapter, we shall consider how these static and dynamic quantities are related to each other and how microscopic properties of the system such as the bond angle distribution give us an insight into anomalous properties. Finally, we shall relate the effects of the variation of the polarisability to real materials.

7.1 Motivation from Liquid Water

The method followed in this project in studying the relationship between different anomalous properties was first proposed by Errington and Debenedetti in their study of the relationship between structural order and anomalies found in liquid water [15]. They summarised all the different anomalous properties into a single plot (Figure 7.1). Structural anomalies, where disorder increases upon compression, occurs over the broadest range of temperatures and densities. Diffusive anomalies, where the diffusion coefficient increases upon compression, occur entirely inside the structurally anomalous region. Finally, thermodynamic anomalies, where the density increases upon heating, occurs at the most restrictive range—entirely inside the area of both structural and diffusive anomalies.

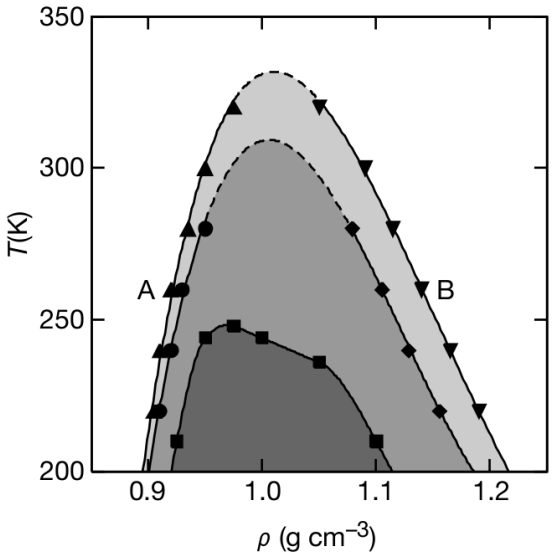

Figure 7.1: Cascade of Anomalies for liquid water[3]. The innermost region (darkest), bounded by the TMD line (squares), is the thermodynamically anomalous region, i.e., density increases upon heating at constant pressure. The further region, bounded by the line of diffusivity minima (circles) and maxima (diamonds), and also including the inner region, possesses the diffusive anomaly, i.e., D increases upon compression. Finally, the outermost region (lightest), bounded by the line of q-maxima (upward-pointing triangles) and t-minima (downward-pointing triangles), and also including the inner two regions, possesses the structural anomaly, i.e., water becomes more disordered upon compression.

7.2 Cascade of Anomalies

In order to create a cascade of anomalies, similar to that of water (Figure 7.1), the regions of thermodynamic anomalies (Figure 3.7), structural anomalies (Figure 4.19), and diffusive anomalies (Figure 5.7) are plotted into a single ρ–T plane, for each value of anion polarisability. Figures 7.2 and 7.3 present the cascades of anomalies for network-forming liquid with polarisability values of 0 and 5 a.u., respectively. Each figure consists of three lines which define the three regions: thermodynamic (black), diffusive (red), and structural (blue) anomalous regions.

[3]The figure is reproduced from [15].

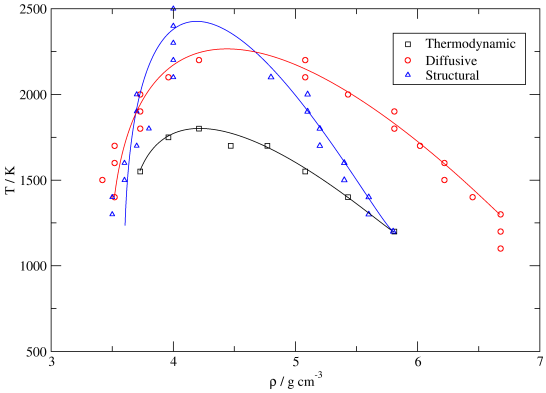

Figure 7.2: Cascade of Anomalies for $\alpha = 0$ a.u. Lines indicate the regions of thermodynamic (black), diffusive (red), and structural (blue) anomalies.

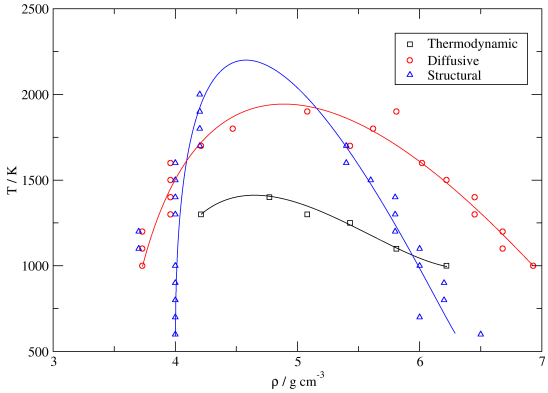

Figure 7.3: Cascade of Anomalies for $\alpha = 5$ a.u. The key is as for Figure 7.2.

To analyse the problem more quantitatively, following the method used by Jabes *et al* [20], who extended the work on water [15], we scale the density by an appropriate length scale, i.e., $\rho^* = \rho\sigma_{\mathrm{AA}}^3$, where $\sigma_{\mathrm{AA}} = 4.07\,\mathring{A}$ is the position of the first peak of the anion–anion radial distribution function measured at the lowest temperature and density for each value of anion polarisability, and the temperature by the melting point at atmospheric pressure, $T_m = 591$ K [53]. Table 7.1 summarises the values of density and temperature at the maximum of each line. All the density and temperature maxima for the two polarisabilities are quite similar in each anomalous category. We postpone the discussion and comparison with other materials to the next section.

The two cascades are essentially the same in shapes and in relative positions of the regions of anomalies: the innermost region is that of thermodynamic anomalies (bounded by the black line), the two outer regions—that of structural (blue) and diffusive (red) anomalies—are intertwined with most of structural anomalies being inside diffusive anomalies. The polarisability dependence is reflected on the positions of the cascades on the ρ–T plane. The increase in polarisability results in the cascade being moved to a lower T and higher ρ. Since this phenomenon occurs similarly with all anomalous properties, these different properties must not be independent from one another and might stem from the same origin.

Units	Thermodynamic		Diffusive		Structural	
	$\rho_{\max}^{\mathrm{TMD}}$	$T_{\max}^{\mathrm{TMD}}$	$\rho_{\max}^{D}$	$T_{\max}^{D}$	$\rho_{\max}^{tq}$	$T_{\max}^{tq}$
$\alpha = 0$ a.u. (RIM)						
original	4.2	1800	4.3	2260	4.2	2420
scaled	1.26	3.05	1.29	3.82	1.26	4.09
$\alpha = 5$ a.u.						
original	4.7	1410	4.9	1930	4.6	2200
scaled	1.40	2.39	1.46	3.27	1.37	3.72

Table 7.1: Densities and temperatures at the maximum of each line of anomaly. The corresponding values are given in both the original units, g cm^{-3} for densities and K for temperatures, and the scaled units, $\sigma_{\mathrm{AA}}^{-3}$ for densities and T_m for temperatures, where $\sigma_{\mathrm{AA}} = 4.07\,\mathring{A}$ is the position of the first peak of the anion–anion radial distribution function measured at the lowest temperature and density and $T_m = 591$ K is the melting point at atmospheric pressure.

7.3 Discussion and Conclusions

In Section 3.2, we have found that increasing anion polarisability effectively decreases the magnitude of bond angles and increases the number of edge-sharing tetrahedral units. In the previous section, we have also found that increasing anion polarisability moves the regions of anomalies of all types to higher density and lower temperature, below the system melting point, that is to within the supercooled region. As a result, the higher the value of polarisability, the more difficult it is to observe the anomalous behaviour. Therefore, we can relate the smaller bond angles and the increasing number of edge-sharing tetrahedral units to supressed anomalous behaviour.

In order to compare our results to other types of materials, we compare the cascades of anomalies of our network-forming materials that are meant to model $ZnCl_2$, except the varying anion polarisabilities, to the cascades of anomalies of other compounds in earlier studies. Figure 7.4 presents the cascades of anomalies for four network-forming liquids: (a) GeO_2 [20], (b) BeF_2 [20], (c) silica [38], and (d) water [15]. Jabes *et al* simulate the three ionic melts by using the Rigid-

Ion Model [52], specifically, by using OE [28] for GeO_2, TRIM for BeF_2, and BKS [22, 44] for silica. Water is modelled by using the three-site rigid-body Extended Simple Point-Charge (SPC/E) model [3]. It is clear that the shapes of the cascades of anomalies do vary for different compounds. However, an eminent feature is that all cascades are nested. In addition, the regions of thermodynamic anomalies, bounded by the TMD lines, are always innermost—inside the regions of diffusive and structural anomalies. According to Jabes *et al* [20], the regions of structural anomalies vary appreciably because the interplay between between thermal disorder, local tetrahedral constraints, and all the ion correlations are relatively complicated. Furthermore, Jabes found that the temperatures at maximum of any types of anomalies are very similar for GeO_2 and water, and are approximately 0.9–1.4 T_m, whereas those for BeF_2 and sicila are also very similar but are approximately 2.8–3.1 T_m. All the temperatures at maximum relative to T_m decreases in the following sequence: $BeF_2 > SiO_2 > GeO_2 > H_2O$. Finally, the $T^{tq}_{\max}/T^{D}_{\max}$ ratios are in between 1.0–1.2 and the $T^{\mathrm{TMD}}_{\max}/T^{D}_{\max}$ ratios are approximately 0.8, for SiO_2, GeO_2, H_2O; the data for BeF_2 is not available.

Since the models used to simulate these four systems are very different, it is difficult to attribute the nature of the differences of these cascades of anomalies to a specific feature of the compounds. The advantage of using the PIM is that all other parameters, except the anion polarisability, are kept fixed. We, therefore, can study the anomalous properties in a systematic way.

Based on the results presented, we found that the anion polarisability affects the microscopic nature of the materials in that the increase in the polarisability causes the average bond angle to decrease. It also affects the cascades of anomalies in that they move all the anomalous regions to the lower temperature and higher density, which is towards the supercooled regime of the phase diagram. The variation of the polarisability, however, does not affect the shape and the order of anomalies in the cascades. By comparing our results (Figure 7.2 and 7.3) to those previously studied (Figure 7.4), we found that the cascades of anomalies for our simulations are very similar to that of BeF_2 and SiO_2, with the TMD line being innermost, and the line of order parameter extrema and the line of diffusive extrema lie outside and are very close to each other. An additional piece of evidence that supports that our PIM is somewhat similar to SiO_2 and BeF_2 is

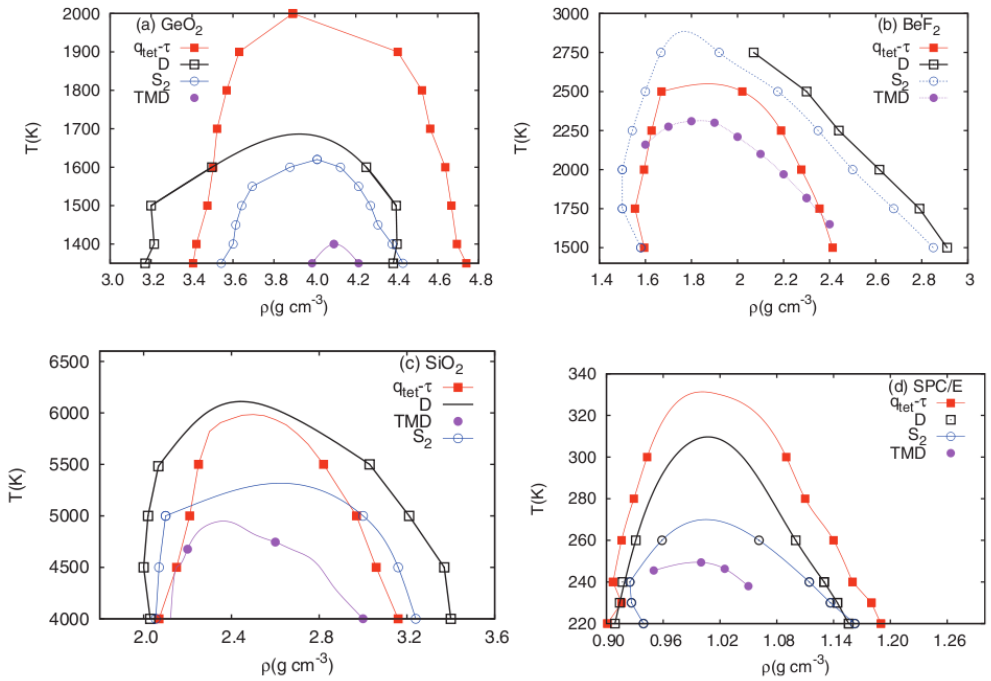

Figure 7.4: Cascade of Anomalies for (a) GeO_2, (b) BeF_2, (c) SiO_2, and (d) H_2O[4]. Each cascade contains regions of structural (red), diffusive (black), and thermodynamic (purple) anomalies. In addition, it also contains regions of anomalous pair entropy (blue), a property not investigated in this study.

that all the temperatures at maximum ($T_{\max}$) from our model (Table 7.1), 3.0–4.1 T_m for RIM and 2.4–3.7 T_m for $\alpha = 5$ a.u., are closer to the values of BeF_2 and GeO_2 (2.8–3.1 T_m), compared to those of GeO_2 and SiO_2 (0.9–1.4 T_m). The ratios $T^{tq}_{\max}/T^{D}_{\max} = 1.1$ and $T^{\mathrm{TMD}}_{\max}/T^{D}_{\max} = 0.8$ and 0.7, for $\alpha = 0$ and 5 a.u., from our simulations also agree very well with the values found in earlier studies [20].

We note also that the relationship between the anomalous properties observed for GeO_2 appear significantly different to those observed for either SiO_2, BeF_2. According to Figure 7.4, whilst the cascades of anomalies for SiO_2 and BeF_2 have the TMD line being innermost, followed by the line of structural anomalies and the line of anomalous diffusivity, that for GeO_2 has the TMD line being innermost as well, but having the order of line of anomalous diffusivity and the line of structural anomalies switched. In addition, if the temperature of each compound is scaled by T_m [20], the melting temperature at 1 atm pressure, it is also found that the maximum temperatures on the TMD lines, $T^{\mathrm{TMD}}_{\max}$, are approximately $2.5T_m$ for both SiO_2 and BeF_2, but is approximately $0.95T_m$ for GeO_2. Similarly, the maximum temperatures on the lines of structural anomalies, $T^{\mathrm{str}}_{\max}$, are approximately $3T_m$ for SiO_2 and BeF_2, but is $1.4T_m$ for GeO_2. Therefore, this is interesting since we might imagine that, in the context of the models presented here, GeO_2 were simply related to SiO_2 (a viewpoint supported, for example, by the more acute Ge–O–Ge bond angle and pressure-induced structural changes). It is, thus, possible that the significant differences observed for SiO_2 and GeO_2, using potentials well-suited to modelling these specific systems, are associated with more subtle differences in the forms of those potential models. Future work will focus on an effective transformation from SiO_2 to GeO_2 to investigate these trends. We note, however, that the behaviour of the TMD line, on moving from SiO_2 to GeO_2, is reflected in the current results. As the polarisability is increased, and the average M–X–M bond angle decreased, the maximum in the TMD line moves to lower T (eventually moving into the supercooled regime). Analogously, behaviour is observed for the SiO_2 and GeO_2 models.

Since polarisability variation does not lead to different relative positions of the cascades whilst cascades of different compounds have different relative positions, perhaps, this is a result of the different strength and nature of the interaction

[4]The figure is exactly reproduced from [20].

between the cations and the anions. In terms of simulation parameters, it is possible that the relative positions of the cascades of anomalies can be changed only by varying other details of the model, for instance, the formal charges of the ions or parameters in the Fumi–Tosi part of the potential model. Furthermore, the cascades of anomalies of the three compounds are very different from that of water. Due to the very different nature of inter-particle interactions—strong ionic interactions with covalent character for ionic melts and much weaker hydrogen bond for water molecules—it is not very surprising that the behaviour of cascades of anomalies of two sets of compounds are very different. If we wish to study the dependence of cascades of anomalies on the nature of different compounds, other system of parameters is required to be investigated in order to locate the cause of changes in the order of anomalous regions in the cascades of anomaly.

Furthermore, whilst the anion polarisability controls the M–X–M bond angles, it is also clear that the systematic variation of this single parameter has additional effects. For example, the number of coordination defects (non-4-coordinated sites) and the associated structural metrics (q and t) appear to be relatively strong functions of the polarisability, and clearly, the locations of the anomalies in ρ–T plane are highly sensitive to these structural properties. It is, therefore, difficult to fully untangle the effect of the anion polarisability in terms of changing the network topology (intermediate-range order) through the control of M–X–M bond angles and in terms of affecting the nearest-neighbour (short-range) orderings. Future work will focus on moving along constant structural metric surfaces in order to probe these differences.

References

[1] N. W. Ashcroft and N. D. Mermin. *Solid State Physics*. Brooks/Cole (1976).

[2] P. Ball. *Life's Matrix. A biography of Water*. University of California Press, Berkeley (2001).

[3] H. J. C. Berendsen, J. R. Grigera, and T. P. Straatsma. The missing term in effective pair potentials. *J. Phys. Chem.*, 91, 6269–6271 (1987).

[4] J. D. Bernal. An attempt at a molecular theory of liquid structure. *Trans. Farad. Soc.*, 67, 27–40 (1937).

[5] J. D. Bernal. A geometrical approach to the structure of liquids. *Nature*, 183, 141–147 (1959).

[6] A. B. Bhatia and D. E. Thornton. Structural aspects of the electrical resistivity of binary alloys. *Phys. Rev. B*, 2, 3004–3012 (1970).

[7] V. Brazhkin, Y. Katayama, A. Lyapin, S. Popova, Y. Inamura, H. Saitoh, and W. Utsumi. Structural studies of phase transitions in crystalline and liquid halides ($ZnCl_2$, $AlCl_3$) under pressure. *JETP Lett.*, 82, 713–718 (2005).

[8] A. D. Buckingham. Permanent and induced molecular moments and long-range intermolecular forces. *Adv. Chem. Phys.*, 12, 107–142 (1967).

[9] R. Car and M. Parrinello. Unified approach for molecular dynamics and density-functional theory. *Phys. Rev. Lett.*, 55, 2471–2474 (1985).

[10] P. M. Chaikin and T. C. Lubensky. *Principles of Condensed Matter Physics*. Cambridge University Press (2000).

[11] P.-L. Chau. Curvature effects on hydrophobic solvation. *Mol. Phys.*, 89, 1033–1055 (1996).

[12] P.-L. Chau and A. J. Hardwick. A new order parameter for tetrahedral configurations. *Mol. Phys.*, 93, 511–518 (1998).

[13] A. M. R. de Graff and M. F. Thorpe. The long-wavelength limit of the structure factor of amorphous silicon and vitreous silica. *Acta Cryst. A*, 66, 22–31 (2010).

[14] C. Domene, P. W. Fowler, M. Wilson, and P. A. Madden. A transferable representation of the induced multipoles in ionic crystals. *Mol. Phys.*, 100, 3847–3865 (2002).

[15] J. R. Errington and P. G. Debenedetti. Relationship between structural order and the anomalies of liquid water. *Nature*, 409, 318–321 (2001).

[16] T. E. Faber and J. M. Ziman. A theory of the electrical properties of liquid metals. *Phil. Mag.*, 11, 153–173 (1965).

[17] A. Gray-Weale, P. A. Madden, and M. Wilson. Induced-dipole contributions to the conductivity and dielectric response of molten $ZnCl_2$. *J. Chem. Phys.*, 113, 6782–6787 (2000).

[18] J.-P. Hansen and I. R. McDonald. *Theory of Simple Liquids*. Academic Press, 3 edition (2006).

[19] T. Hill. *Statistical Mechanics: Principles and Selected Applications*. Dover Books on Physics Series. Dover Publications (1987).

[20] B. S. Jabes, M. Agarwal, and C. Chakravarty. Tetrahedral order, pair correlation entropy, and waterlike liquid state anomalies: Comparison of GeO_2 with BeF_2, SiO_2, and H_2O. *J. Chem. Phys.*, 132, 234507 (2010).

[21] R. E. Kirk and D. F. Othmer. *Encyclopedia of Chemical Technology*. Wiley, New York (1992).

[22] G. J. Kramer, N. P. Farragher, B. W. H. van Beest, and R. A. van Santen. Interatomic force fields for silicas, aluminophosphates, and zeolites: Derivation based on *ab initio* calculations. *Phys. Rev. B*, 43, 5068–5080 (1991).

[23] P. A. Madden and M. Wilson. 'Covalent' effects in 'ionic' systems. *Chem. Soc. Rev.*, 25, 339–350 (1996).

[24] P. A. Madden and M. Wilson. 'Covalent' effects in 'ionic' liquids. *J. Phys.: Condens. Matter*, 12, A95–A108 (2000).

[25] D. A. Mcquarrie. *Statistical Mechanics*. University Science Books (2000).

[26] O. Mishima, L. D. Calvert, and E. Whalley. 'Melting ice' I at 77 K and 10 kbar: a new method of making amorphous solids. *Nature*, 310, 393–395 (1984).

[27] O. Mishima, L. D. Calvert, and E. Whalley. An apparently first-order transition between two amorphous phases of ice induced by pressure. *Nature*, 314, 76–78 (1985).

[28] R. D. Oeffner and S. R. Elliott. Interatomic potential for germanium dioxide empirically fitted to an *ab initio* energy surface. *Phys. Rev. B*, 58, 14791–14803 (1998).

[29] P. H. Poole, F. Sciortino, U. Essmann, and H. E. Stanley. Phase behaviour of metastable water. *Nature*, 360, 324–328 (1992).

[30] P. H. Poole, F. Sciortino, U. Essmann, and H. E. Stanley. Spinodal of liquid water. *Phys. Rev. E*, 48, 3799–3817 (1993).

[31] M. C. C. Ribeiro, M. Wilson, and P. A. Madden. The nature of the "vibrational modes" of the network-forming liquid $ZnCl_2$. *J. Chem. Phys.*, 109, 9859–9869 (1998).

[32] J. J. Salacuse, A. R. Denton, and P. A. Egelstaff. Finite-size effects in molecular dynamics simulations: Static structure factor and compressibility. i. theoretical method. *Phys. Rev. E*, 53, 2382–2389 (1996).

[33] P. S. Salmon. The structure of molten and glassy 2:1 binary systems: An approach using the bhatia-thornton formalism. *Proc. R. Soc. Lond. A*, 437, 591–606 (1992).

[34] P. S. Salmon. Moments of the Bhatia–Thornton partial pair-distribution functions. *J. Phys.: Condens. Matter*, 17, S3537–S3542 (2005).

[35] M. Sangster and M. Dixon. Interionic potentials in alkali halides and their use in simulations of the molten salts. *Adv. Phys.*, 25, 247–342 (1976).

[36] S. Sastry, P. G. Debenedetti, F. Sciortino, and H. E. Stanley. Singularity-free interpretation of the thermodynamics of supercooled water. *Phys. Rev. E*, 53, 6144–6154 (1996).

[37] B. K. Sharma and M. Wilson. Intermediate-range order in molten network-forming systems. *Phys. Rev. B*, 73, 060201 (2006).

[38] M. S. Shell, P. G. Debenedetti, and A. Z. Panagiotopoulos. Molecular structural order and anomalies in liquid silica. *Phys. Rev. E*, 66, 011202 (2002).

[39] R. J. Speedy. Limiting forms of the thermodynamic divergences at the conjectured stability limits in superheated and supercooled water. *J. Phys. Chem.*, 86, 3002–3005 (1982).

[40] R. J. Speedy. Stability-limit conjecture. an interpretation of the properties of water. *J. Phys. Chem.*, 86, 982–991 (1982).

[41] P. J. Steinhardt, D. R. Nelson, and M. Ronchetti. Bond-orientational order in liquids and glasses. *Phys. Rev. B*, 28, 784–805 (1983).

[42] S. Torquato and F. H. Stillinger. Local density fluctuations, hyperuniformity, and order metrics. *Phys. Rev. E*, 68, 041113 (2003).

[43] T. M. Truskett, S. Torquato, and P. G. Debenedetti. Towards a quantification of disorder in materials: Distinguishing equilibrium and glassy sphere packings. *Phys. Rev. E*, 62, 993–1001 (2000).

[44] B. W. H. van Beest, G. J. Kramer, and R. A. van Santen. Force fields for silicas and aluminophosphates based on *ab initio* calculations. *Phys. Rev. Lett.*, 64, 1955–1958 (1990).

[45] G. F. Voronoï. Nouvelles applications des paramètres continus à la théorie des formes quadratiques. *J. Reine Angew. Math.*, 198–287 (1908).

[46] M. Wilson and P. A. Madden. Polarization effects in ionic systems from first principles. *J. Phys.: Condens. Matter*, 5, 2687–2706 (1993).

[47] M. Wilson and P. A. Madden. "prepeaks" and "first sharp diffraction peaks" in computer simulations of strong and fragile ionic liquids. *Phys. Rev. Lett.*, 72, 3033–3036 (1994).

[48] M. Wilson and P. A. Madden. Voids, layers, and the first sharp diffraction peak in $ZnCl_2$. *Phys. Rev. Lett.*, 80, 532–535 (1998).

[49] M. Wilson and P. A. Madden. α and β relaxation processes in $ZnCl_2$—a computer simulation study. *J. Phys.: Condens. Matter*, 11, A237–A246 (1999).

[50] M. Wilson, P. A. Madden, and B. J. Costa-Cabral. Quadrupole polarization in simulations of ionic systems: Application to agcl. *J. Phys. Chem.*, 100, 1227–1237 (1996).

[51] M. Wilson and P. S. Salmon. Network topology and the fragility of tetrahedral glass-forming liquids. *Phys. Rev. Lett.*, 103, 157801 (2009).

[52] L. V. Woodcock, C. A. Angell, and P. Cheeseman. Molecular dynamics studies of the vitreous state: Simple ionic systems and silica. *The Journal of Chemical Physics*, 65, 1565–1577 (1976).

[53] A. C. Wright, G. Etherington, J. Desa, R. N. Sinclair, G. Connell, and J. M. Jr. Neutron amorphography. *J. Non-Crys. Sol.*, 49, 63 – 102 (1982).